LLNL-JRNL-787828

Topology Optimization of Multiple Deformable Bodies in Contact

L. F. Fernandez, M. Puso, J. Solberg, D. A. Tortorelli

August 22, 2019

Computer Methods in Applied Mechanics and Engineering

Topology Optimization of Multiple Deformable Bodies in Contact with Large Deformations

Felipe Fernandez[a,b,*], Michael A. Puso[b], Jerome Solberg[b], Daniel A. Tortorelli[a,b]

[a] *Department of Mechanical Sciences and Engineering, University of Illinois at Urbana-Champaign, Illinois, USA*
[b] *Lawrence Livermore National Laboratory, California, USA*

Abstract

Previous works in topology optimization of structures with contact boundary conditions have concentrated on the two-dimensional rigid obstacle problem. This is because the contact analysis of multiple three-dimensional deformable bodies with meshes that are non-matching across the contact interface requires computationally complex contact algorithms beyond the scope of previous optimization investigations. Our research is devoted to addressing topology design problems with multiple deformable three-dimensional components in contact using state-of-the-art contact algorithms.

We formulate and resolve the design simulation problem using *large deformation* continuum mechanics and the finite element method. To account for *large sliding* that can occur during the design optimization process here, the mortar segment-to-segment approach was used to discretize the contact surface due to its numerical robustness in this regime. Since, mortar integrals provide smooth contact forces as nodes slide on/off the surface, solution convergence is well behaved. Considering the contact problem is computationally expensive to solve, we solve the optimization problem using efficient nonlinear programming algorithms which require the sensitivities of the cost and constraint functions. To this end, we formulate analytical adjoint sensitivity expressions to compute the gradients of general functionals. As expected and corroborated in this work, the adjoint method is computationally efficient. Additionally, we use a B-spline design parameterization to regularize the topology optimization problem. We show that this parameterization reduces the number of design variables compared to usual element-wise parameterizations and provides a precise and smooth description of the design boundary. We present numerical example problems of multiple deformable three-dimensional bodies in contact with large deformations and find optimal topologies that maximize the total contact force, maximize the strain energy, and minimize the compliance.

Keywords: Finite elements, Large deformation, Mortar segment-to-segment, Sensitivity analysis, B-spline

---

1. Introduction

Appropriate modeling of the boundary conditions is crucial to the design of structural components. Indeed, poor modeling results in poor designs with potentially catastrophic consequences. Of these boundary conditions, contact is the one that dominates countless physical situations, e.g., crashworthiness, wear and lubrication, metal forming, braking systems, tires, coupling devices, geomechanics, hardening testing, ballistics, etc. [1]. It is present in all structural simulations. However, contact modeling is challenging so these boundary conditions are often replaced by simple traction and/or displacement boundary conditions which compromise the accuracy of the simulation and hence the validity of the design. We propose to optimize structural components in contact by combining accurate contact modeling techniques with efficient optimization algorithms.

---

[*] Corresponding author

Email addresses: `lfferna2@illinois.edu` (Felipe Fernandez), `puso1@llnl.gov` (Michael A. Puso), `solberg2@llnl.gov` (Jerome Solberg), `tortorelli2@llnl.gov` (Daniel A. Tortorelli)

Preprint submitted to Computer Methods in Applied Mechanics and Engineering *July 22, 2020*

Despite the dominant role of contact in structural analysis, it is rarely modeled because it poses serious conceptual, mathematic, and computational difficulties [2]. Indeed, the contact surfaces are unknown as are the resulting contact pressures and displacements over these surfaces. Moreover, the contact pressure must be compressive and the displacement must satisfy impenetrability constraints. These pressure and impenetrability conditions make the contact problem particularly difficult to solve as the computational analysis must resolve inequality constraints as well as the usual elasticity equations [2]. The presence of friction makes the problem even more complex. Fortunately, several numerical techniques have been developed to model contact efficiently and accurately, cf. [2–6].

The Signorini problem, i.e., a linear elastic body in contact with a rigid obstacle, has been extensively studied [2]. Other early contact modeling works focused on the frictionless contact between linear elastic bodies. Researchers eventually studied the large deformations of inelastic contacting bodies with friction. To solve the contact problem numerically, the strong form of the equilibrium equation with the added contact conditions are converted to an equivalent weak form which takes the form of a variational inequality. The penalty method (PM) is often used to convert the variational inequality to an equality which is more amenable to solution [2]. Unfortunately, the PM allows for small violations of the interpenetration constraint. A large penalty parameter reduces the amount of this constraint violation, however, over-penalization leads to numerical ill-conditioning. Alternatively, in the classical Lagrange multiplier method (LMM), the contact conditions are satisfied exactly by introducing extra degrees of freedom, i.e., Lagrange multipliers. Introducing these unknowns makes the problem more expensive to solve in comparison with the PM. Moreover, the LMM method requires an active set strategy to update active inequality constraints. The augmented Lagrangian method (ALM) resolves these shortcomings by combining the PM and the LMM. It satisfies the contact conditions exactly and uses a reasonable value for the penalty parameter. Both the PM and ALM are available in commercial finite element software [6]. In our work, we apply the ALM since it avoids indefinite systems of equations which can be a problem for many linear solvers. It also works expeditiously within a Quasi-Newton solution scheme using direct solvers. Additionally, as presented in Section 4 and demonstrated in Section 7, we can nonetheless formulate efficient sensitivity analysis.

When modeling multiple deformable bodies in contact with the finite element method, meshes of each body generally do not align over the contact surface. Several approaches are adopted to integrate the contact conditions over such nonconforming interfaces. The node-on-segment approach enforces the contact constraint using collocation such that nodes on the “slave” surface must not penetrate the element faces of the opposing “master” surface [7]. This approach is plagued by variational inconsistency (failure to pass the patch test), locking in the two-pass variant and abrupt jumps in the contact pressure. These issues are resolved by the mortar segment-to-segment method, where the contact constraint is enforced in an integral sense, via projection of the slave onto the mating element faces on the master surface [8, 9]. The mortar segment-to-segment method is less dependent to the master and slave surface designations and does not exhibit large contact pressure fluctuations.

The eXtended Finite Element Method (XFEM) has shown great promise to model friction and sliding contact [10]. In this approach, the displacement field is augmented by enrichment functions to capture discontinuities. The primary advantage of the XFEM method is that it does not require a conforming mesh over the body, and in particular the contact surface. But like all methods, it has disadvantages, namely ill-conditioning due to interpolation over small and irregularly shaped sub domains [11]. However, these issues can be resolved by implementing stabilization methods [12, 13].

Much research has focused on the optimal design of linear elastic structures in contact with a rigid obstacle, cf. the extensive survey by Hilding et al. [14]. Sizing, shape and Topology Optimization (TO) problems have been solved to minimize the peak contact pressure, obtain a uniform pressure, maximize stiffness, reduce weight, etc.

Topology optimization of structures subjected to contact have been formulated using different contact models and/or optimization approaches. Klarbring et al. [15] solve truss TO design problems that include unilateral contact boundary conditions. In this work, the design variables are the volumes of the bars and the initial gaps between the contact nodes and the rigid obstacle. Petersson and Patriksson [16] apply TO to design continuum structures in contact. To overcome the non-differentiability issues associated with the contact constraints, they use a subgradient optimization algorithm and compute the optimal design as an average of the candidate designs that are generated in the subgradient calculations. Li [17] uses an evolutionary approach to design linear elastic frame structures in contact. Fancello [18] combines the Solid Isotropic Material with Penalization (SIMP) approach [19] and the ALM for the TO of structures in contact subject to stress constraints. They assume differentiability and compute analytical sensitivities using the adjoint method. The optimized designs are highly dependent on the initial design choice. This nonuniqueness is attributed to the lack of differentiability of the contact problem as different contact surfaces exist for each initial design resulting in drastically different sensitivities, which drive the optimization to different local solutions.

Desmorat [20] models frictionless unilateral contact in the TO of continuum structures assuming the contact pressure is derived from a potential function. Strömberg and Klarbring [21–24] compared topology optimized designs obtained using Facchinei's smoothing and augmented Lagrangian contact formulations. They report that the latter is slightly more efficient. It is worth noting that [23] includes three-dimensional examples and [24] considers an adjustable compliance-volume product as the cost function. Strömberg extended this approach to the TO of structures exhibiting frictional contact with a rigid support [25]. Meanwhile Bruggi and Duysinx [26] designed structures in unilateral contact by enforcing the contact conditions via stress constraints over the contact surface. Luo et al. [27] use nonlinear springs to model frictionless contact in the TO of hyperelastic structures.

TO has also been used to design compliant mechanisms which exhibit contact. Mankame and Ananthasuresh [28] use a cross-constraint method, similar to the PM, to design mechanisms made of frame elements; they extend this work to include large deformation in [29]. Kumar et al. [30] use circular masks to define the material and rigid surface regions, and zero-order optimization algorithms to design 2D mechanisms. This work is extended to include self-contact in [31].

TO problems of structures under contact have also been solved using the topological derivative in combination with the level-set method [32–34]. Andrade-Campos et al. [35] use this approach to study the remodeling behavior of bone, and Myśliński extends it to include friction [36, 37]. In [38], Lawry and Maute combine an explicit level-set method with the XFEM to optimize multiple deformable bodies in contact. This work was extended to design linear elastic contacting bodies in three-dimensions [39], and nonlinear contacting bodies in two-dimensions [11]. These works do not use body fitted meshes, rather the shape of the contacting surfaces are determined by evolving a well-defined interface via the optimization. Maury et al. [40] combine the level-set method with the PM to shape optimize linear elastic structures in unilateral contact. They consider five different friction models and use a commercially available finite element software for their simulations.

Crashworthiness design is another area that TO has been applied. These design problems model a vehicle and/or body impacting a rigid wall. The designs seek to maximize crash energy absorption and/or occupant safety. These problems face many challenges due to the large computational cost of the analyses that are needed to resolve geometric, material, and contact nonlinearities. Explicit time stepping algorithms are typically used in the simulations as they avoid Newton iterations and their matrix inversion; however they are limited to small time steps which is acceptable in these impact simulations. In an early study, Mayer et al. [41] applied TO to maximize the crash energy absorption in a body rear rail using the homogenization method, explicit time stepping, and the optimality criteria optimization algorithm. Pederson [42–44] uses TO to design frame structures made of plastic beams that exhibit large deformations. This author uses implicit time stepping and computes analytical sensitivities using the direct method. Alternate methods have been adopted to simplify the problems and/or use heuristic non-gradient techniques to update the designs, e.g., the hybrid cellular automata, evolutionary optimization, equivalent static loads, bubble and graph methods [45–50]. For a detailed review of design for crashworthiness, the reader is referred to [51].

The literature review above discusses the most relevant work in the TO of structures in contact. They are primarily restricted to two-dimensional linear elastic bodies in contact with rigid obstacles with the exceptions of:

- [29] which includes large deformation,
- [23, 24, 40] that solve three-dimensional problems with rigid obstacles,

- The crashworthiness studies in [41–50] that include three-dimensional problems with rigid obstacles and geometrical and/or material nonlinearities and
- The design of multi-body structures in contact using XFEM in [11, 38, 39], where the contact surfaces are defined with the level-set method.

As noted, the three-dimensional research is mainly limited to contact with rigid obstacles. XFEM shows great promise to optimize three-dimensional multiple components in contact, but it needs further development to solve problems in the finite strain regime [39].

Our research is devoted to combining TO with the state-of-the-art contact algorithms to design systems with multiple deformable three-dimensional bodies in contact. Since the contact analysis is computationally expensive, we use efficient optimization algorithms which require sensitivity analysis. Novel features of our design optimization work include the use of

- large deformation continuum formulation that is suitable for the arbitrary discretization of three-dimensional contacting bodies,
- the mortar segment-to-segment method [8] to discretize the contact equations and
- a B-spline [52] design parameterization to 1) reduce the number of design variables in comparison to element-wise parameterizations and 2) formulate a well-posed TO problem.

We use body-fitted meshes with known contact mating surfaces, i.e., a priori known master and slave surfaces. Additionally, we use the ALM to enforce the contact constraints, the analytical adjoint sensitivity analysis of general functionals and the Interior Point Optimizer (IPOPT) for the gradient-based optimization algorithm. Finally, we provide numerical examples. To reduce complexity, our study is limited to nonlinear elastic bodies and frictionless contact. Incorporating plasticity and friction will be the focus of our future work.

The remainder of the paper is organized as follows. Section 2 provides the terminology and definitions for the nonlinear elasticity governing equation. In Sections 3–5, we formulate the contact problem and sensitivity analysis and present various solution algorithms. The design optimization problem is presented and examples are provided in Sections 6 and 7. Conclusions are drawn in Section 8.

2. Nonlinear elasticity

The body resides in the initial configuration Ω which is displaced into the deformed configuration ω by the deformation $\boldsymbol{\varphi} : \Omega \to \mathbb{R}^3$, cf. Figure 1. Under this deformation, material particles identified by the reference location $\mathbf{X} \in \Omega$ are displaced to $\mathbf{x} = \boldsymbol{\varphi}(\mathbf{X}) = \mathbf{X} + \mathbf{u}(\mathbf{X})$, where $\mathbf{u}$ is the displacement. As per usual, the deformation gradient is $\mathbf{F} = \nabla\boldsymbol{\varphi} = \mathbf{I} + \nabla\mathbf{u}$, the right Cauchy–Green deformation tensor is $\mathbf{C} = \mathbf{F}^\top\mathbf{F}$ and the Jacobian is $J = \det(\mathbf{F})$.

In the continuum setting we find the displacement field $\mathbf{u}$ such that

$$\begin{aligned} \operatorname{div}\mathbf{P}(\mathbf{F},\nu) + \mathbf{b} &= \mathbf{0} && \text{in } \Omega\,, \\ \mathbf{P}(\mathbf{F},\nu)\,\mathbf{N} &= \mathbf{s}^p && \text{on } A^t\,, \\ \mathbf{u} &= \mathbf{u}^p && \text{on } A^u\,, \end{aligned} \tag{1}$$

where[1] $\mathbf{P}$, $\mathbf{b}$, $\mathbf{s}^p$ and $\mathbf{u}^p$ are the first Piola-Kirchhoff stress, body force, prescribed traction and prescribed displacement fields, and A^t and A^u are complimentary surfaces of $\partial\Omega$. $\mathbf{N}$ is the normal vector to the surface $\partial\Omega$. In this elastic body, the stress $\mathbf{P}$ is a function of the deformation gradient $\mathbf{F}$ and the topology material distribution ν. The latter is known in the elasticity analysis, but unknown in the optimization problem.

---

[1] For conciseness we suppress the spatial dependence on position $\mathbf{X}$ for all fields.

In the weak formulation we find $\mathbf{u} \in \mathcal{W}$ such that

$$r_b(\mathbf{u}, \mathbf{w}) = \int_\Omega \nabla \mathbf{w} \cdot \mathbf{P}(\mathbf{F}, \nu) \, \mathrm{d}V - \int_\Omega \mathbf{w} \cdot \mathbf{b} \, \mathrm{d}V - \int_{A^t} \mathbf{w} \cdot \mathbf{s}^p \, \mathrm{d}A = 0 \tag{2}$$

for all $\mathbf{w} \in \mathcal{W}_0$ where $\mathcal{W}$ and $\mathcal{W}_0$ denote the trial and virtual solution spaces of the displacement field, i.e., $\mathcal{W} = \{\mathbf{u} \in H^1(\Omega) : \mathbf{u} = \mathbf{u}^p \text{ on } A^u\}$ and $\mathcal{W}_0 = \{\mathbf{u} \in H^1(\Omega) : \mathbf{u} = \mathbf{0} \text{ on } A^u\}$, $\mathrm{d}V$ and $\mathrm{d}A$ are the differential volume and surface elements in the reference configuration. For future reference we call r_b the bulk residual.

We solve for $\mathbf{u}$ via Newton's method whereupon we update the current solution guess $\mathbf{u}^I$ to $\mathbf{u}^{I+1} = \mathbf{u}^I + \Delta\mathbf{u}$ where $\Delta\mathbf{u}$ is the solution to the linear problem: find $\Delta\mathbf{u} \in \mathcal{W}_0$ such that

$$\delta r_b(\mathbf{u}^I, \mathbf{w}; \Delta\mathbf{u}) = -r_b(\mathbf{u}^I) \tag{3}$$

for all $\mathbf{w} \in \mathcal{W}_0$. In the above,

$$\delta r_b(\mathbf{u}, \mathbf{w}; \Delta\mathbf{u}) = \int_\Omega \nabla \mathbf{w} \cdot \mathbb{A}(\mathbf{F}, \nu)[\nabla \Delta\mathbf{u}] \, \mathrm{d}V \,, \tag{4}$$

where $\mathbb{A}(\mathbf{F}, \nu) = \partial \mathbf{P}(\mathbf{F}, \nu)/\partial \mathbf{F}$ is the incremental elasticity tensor evaluated at $\mathbf{F}$, $\Delta\mathbf{u}$ is the *finite* displacement increment and $\delta r_b(\mathbf{u}, \mathbf{w}; \Delta\mathbf{u}) = \lim_{\epsilon \to 0} \frac{1}{\epsilon} \left(r_b(\mathbf{u} + \epsilon \, \Delta\mathbf{u}, \mathbf{w}) - r_b(\mathbf{u}, \mathbf{w}) \right)$ is the variation of r at $(\mathbf{u}, \mathbf{w})$ with respect to $\mathbf{u}$ in the *direction* $\Delta\mathbf{u}$.[2] When discretized $\delta r_b(\mathbf{u}, \mathbf{w}; \Delta\mathbf{u})$ is the product of the tangent stiffness matrix and the increment of the nodal displacement vector. This general continuum mechanics formulation allows us to solve large deformation problems for elastic materials. We present the nonlinear material model that is used in this manuscript in Appendix C.

3. Contact

Without loss of generality we assume we have two bodies $\Omega^{(1)}$ and $\Omega^{(2)}$ in contact. We subdivide each body's surface $\partial\Omega^{(i)}$ into three complementary surfaces $A^{u\,(i)}$, $A^{t\,(i)}$ and $\Gamma^{(i)}$; where $\Gamma^{(i)}$ is the surface over which the contacting bodies potentially interact, cf. Figure 1. Typically, no external traction is applied over the deforming contacting surface $\gamma^{(i)}$ however, a traction will be applied when contact is detected via the contact gap constraint. The *continuum* form of the gap constraint is expressed

$$g(\mathbf{x}, \bar{\mathbf{y}}) \leq 0 \text{ for all } \mathbf{x} \in \gamma^{(1)} \text{ and candidate } \bar{\mathbf{y}} \in \gamma^{(2)} \,, \tag{5}$$

where $\mathbf{x} = \boldsymbol{\varphi}^{(1)}(\mathbf{X})$, $\bar{\mathbf{y}} = \boldsymbol{\varphi}^{(2)}(\bar{\mathbf{Y}})$, and $\bar{\mathbf{Y}}$ is defined by the outward normal projection, i.e., $\bar{\mathbf{y}} = \boldsymbol{\varphi}^{(2)}(\bar{\mathbf{Y}})$ is the point established from the projection of $\mathbf{x} = \boldsymbol{\varphi}^{(1)}(\mathbf{X})$ onto $\gamma^{(2)}$ along the outward unit normal $\mathbf{n}^{(1)}(\mathbf{x})$ of the surface defined on $\gamma^{(1)}$ at $\mathbf{x}$. Note that $\bar{\mathbf{y}} \in \gamma^{(2)}$ is a function of $\mathbf{x} \in \gamma^{(1)}$ and $\mathbf{n}^{(1)}$. For notation simplicity, the overline notation, e.g., $\bar{\mathbf{y}}$, is used henceforth to represent such dependencies. The gap constraint function g is further characterized by the following properties:

- If $g(\mathbf{x}, \bar{\mathbf{y}}) = 0$ the points $\mathbf{x} = \gamma^{(1)}$ and $\bar{\mathbf{y}} = \gamma^{(2)}$ are in contact, i.e., $\boldsymbol{\varphi}^{(1)}(\mathbf{X}) = \boldsymbol{\varphi}^{(2)}(\bar{\mathbf{Y}})$.
- If $g(\mathbf{x}, \bar{\mathbf{y}}) < 0$ points $\mathbf{x}$ and $\bar{\mathbf{y}}$ are separated by a gap.
- And finally, if $g(\mathbf{x}, \bar{\mathbf{y}}) > 0$ point $\mathbf{x} \in \omega^{(1)}$ would penetrate $\omega^{(2)}$; violating the constraint (5).

The gap constraint is maintained by a contact pressure λ defined by either a Lagrange multiplier, penalty function or both with the ALM. The inequality constraints defined by the contact gap function and the pressure observe the following Karush-Kuhn-Tucker (KKT) complementary conditions which are necessary for finding a local minimizer of the potential energy [4]

$$g(\boldsymbol{\varphi}^{(1)}, \bar{\boldsymbol{\varphi}}^{(2)}) \leq 0 \,, \qquad \lambda \leq 0 \,, \qquad \lambda \, g(\boldsymbol{\varphi}^{(1)}, \bar{\boldsymbol{\varphi}}^{(2)}) = 0 \,. \tag{6a-c}$$

---

[2] Here and henceforth, the argument after semicolon in the variation represents the direction of the variation.

These (6) conditions hold for all $\mathbf{x} \in \gamma^{(1)}$ and $\bar{\mathbf{y}} \in \gamma^{(2)}$.

Contact surfaces have classically been described by a slave-master side approach where the slave surface $\gamma^{(1)}$ would be constrained to the master surface $\gamma^{(2)}$ in a one sided formulation. Two sided approaches [7] symmetrize this slave-master approach allowing sides $\gamma^{(1)}$ and $\gamma^{(2)}$ to be both slave and master; unfortunately these formulations often suffer from contact locking and pressure oscillations. Furthermore, traditional approaches such as [7] employ a node-on-surface constraint discretization, i.e., the gap constraint (5) is enforced point-wise only at select nodes. These methods are simple to implement but are not consistent and consequently do not satisfy contact patch tests [4].

3.1. Discretized mortar formulation

The mortar contact method enforces the gap constraints weakly resulting in a consistent formulation that satisfies patch tests and also "smooths out" the contact constraints leading to a more stable, accurate and robust formulation. As we will see later, this smoothness also benefits the optimization process. Indeed, as the design change between iterations, the contact constraints change smoothly, and accordingly, the optimization exhibits smooth monotonic convergence.

In the mortar method, the gap function in (7a) measures the projected distance from the slave surface $\gamma^{(1)}$ onto the master surface $\gamma^{(2)}$ along the slave surface normal vector. The contact pressure in (7b) is interpolated from the node A finite element shape function $N_A^{(1)}$ associated with the deformed slave surface $\gamma^{(1)}$, and node A contact pressure λ_A, for each slave surface contact node $A \in [1, \mathcal{N}_c]$.

$$g(\boldsymbol{\varphi}^{(1)}, \bar{\boldsymbol{\varphi}}^{(2)}) = (\boldsymbol{\varphi}^{(1)} - \bar{\boldsymbol{\varphi}}^{(2)}) \cdot \mathbf{n}^{(1)} \,, \tag{7a}$$

$$\lambda(\boldsymbol{\varphi}^{(1)}) = \sum_{A=1}^{\mathcal{N}_c} N_A^{(1)}(\boldsymbol{\varphi}^{(1)})\, \lambda_A \,, \tag{7b}$$

To be clear, in the above, $\bar{\boldsymbol{\varphi}}^{(2)} = \boldsymbol{\varphi}^{(2)}(\bar{\mathbf{Y}})$ is the point on the deformed master surface $\gamma^{(2)}$ established from the projection of the deformed slave surface point $\mathbf{x} = \boldsymbol{\varphi}^{(1)}$ to $\gamma^{(2)}$ along the outward unit normal $\mathbf{n}^{(1)}(\mathbf{x})$. The nodal, i.e., discrete, gap function g_A is computed from the L_2 projection of the gap function in (7a) onto the slave surface, i.e.,

$$\mathrm{g}_A = \int_\gamma N_A^{(1)}(\boldsymbol{\varphi}^{(1)})(\boldsymbol{\varphi}^{(1)} - \bar{\boldsymbol{\varphi}}^{(2)}) \cdot \mathbf{n}^{(1)}(\boldsymbol{\varphi}^{(1)})\, \mathrm{d}a \,. \tag{8}$$

The nodal gaps g_A and nodal pressures λ_A must satisfy the discrete KKT conditions (6)

$$\mathrm{g}_A \leq 0 \,, \qquad \lambda_A \leq 0 \,, \qquad \lambda_A\, \mathrm{g}_A = 0 \,. \tag{9a-c}$$

These quantities are also used to define the discretized contact virtual work which will be employed in the contact weighted residual r_c in what follows, i.e.,

$$\begin{aligned} \int_\gamma \lambda\, \delta g(\boldsymbol{\varphi}^{(1)}, \bar{\boldsymbol{\varphi}}^{(2)}; \mathbf{w}^{(1)}, \mathbf{w}^{(2)})\, \mathrm{d}a &= \int_\gamma \lambda\, \mathbf{n}^{(1)}(\boldsymbol{\varphi}^{(1)}) \cdot (\mathbf{w}^{(1)} - \bar{\mathbf{w}}^{(2)})\, \mathrm{d}a \\ &= \int_\gamma \sum_{A=1}^{\mathcal{N}_c} N_A^{(1)}(\boldsymbol{\varphi}^{(1)})\, \lambda_A\, \mathbf{n}^{(1)}(\boldsymbol{\varphi}^{(1)}) \cdot (\mathbf{w}^{(1)} - \bar{\mathbf{w}}^{(2)})\, \mathrm{d}a \\ &= \sum_{A=1}^{\mathcal{N}_c} \lambda_A\, \delta \mathrm{g}_A(\boldsymbol{\varphi}^{(1)}, \bar{\boldsymbol{\varphi}}^{(2)}; \mathbf{w}^{(1)}, \mathbf{w}^{(2)}) \,, \end{aligned} \tag{10}$$

where $\mathbf{w}^{(i)}$ is the weighting displacement for surface i and $\bar{\mathbf{w}}^{(2)} = \mathbf{w}^{(2)}(\bar{\boldsymbol{\varphi}}^{(2)})$ and $\delta g(\boldsymbol{\varphi}^{(1)}, \bar{\boldsymbol{\varphi}}^{(2)}; \mathbf{w}^{(1)}, \mathbf{w}^{(2)}) = \lim_{\epsilon \to 0} \frac{1}{\epsilon} \left(g(\boldsymbol{\varphi}^{(1)} + \epsilon\, \mathbf{w}^{(1)}, \bar{\boldsymbol{\varphi}}^{(2)} + \epsilon\, \mathbf{w}^{(2)}) - g(\boldsymbol{\varphi}^{(1)}, \bar{\boldsymbol{\varphi}}^{(2)}) \right)$ is the variation of g at $(\boldsymbol{\varphi}^{(1)}, \bar{\boldsymbol{\varphi}}^{(2)})$ in the direction $(\mathbf{w}^{(1)}, \mathbf{w}^{(2)})$. It should be noted that the form of Equation (10) is an approximation to the extent that $\delta \int_\gamma \lambda\, g\, \mathrm{d}a \approx \int_\gamma (\lambda\, \delta g + \delta\lambda\, g)\, \mathrm{d}a$ for large kinematics considering that $g = 0$ as per Equation (9c). This is to avoid expensive derivative calculations of the surface variation $\delta\gamma$ for three dimensional implementations [8, 53, 54].[3] Finally, the implementation in this work exploits the segment-based integration [8] of (10) in lieu of the element-based integration as discussed in [54]. Details regarding the derivation of the consistent tangent for this formulation are provided in [8]. For conciseness, we henceforth reduce the notation of $g(\boldsymbol{\varphi}^{(1)}, \bar{\boldsymbol{\varphi}}^{(2)})$ and $\delta g(\boldsymbol{\varphi}^{(1)}, \bar{\boldsymbol{\varphi}}^{(2)}; \mathbf{w}^{(1)}, \mathbf{w}^{(2)})$ to $g(\boldsymbol{\varphi})$ and $\delta g(\boldsymbol{\varphi}; \mathbf{w})$.

3.2. Weak form of equations of motion with contact virtual work

Using (7) and (10), the contact constraint is incorporated into the elasticity equations where we now find $\mathbf{u}^{(i)} \in \mathcal{W}$ and $\lambda \in L^2$ such that

$$\begin{aligned} r(\mathbf{u}, \lambda, \mathbf{w}, \beta) = 0 \quad &= \quad \sum_{i=1}^{2} \left[\int_{\Omega^{(i)}} \nabla \mathbf{w}^{(i)} \cdot \mathbf{P}(\mathbf{F}^{(i)}, \nu)\, \mathrm{d}V - \int_{\Omega^{(i)}} \mathbf{w}^{(i)} \cdot \mathbf{b}^{(i)}\, \mathrm{d}V - \int_{A^{t\,(i)}} \mathbf{w}^{(i)} \cdot \mathbf{s}^{p\,(i)}\, \mathrm{d}A \right] + \\ &\qquad \int_{\gamma} \lambda\, \delta g(\boldsymbol{\varphi}; \mathbf{w})\, \mathrm{d}a + \int_{\gamma} \beta\, g(\boldsymbol{\varphi})\, \mathrm{d}a \\ &= \quad r_b(\mathbf{u}, \mathbf{w}) + r_c(\mathbf{u}, \lambda, \mathbf{w}, \beta) \end{aligned} \tag{11}$$

for all $\mathbf{w}^{(i)} \in \mathcal{W}_0$ and $\beta \in L^2$. For conciseness, the bulk residual includes the contributions of each body, i.e., $r_b(\mathbf{u}, \mathbf{w}) = \sum_{i=1}^{2} r_{bi}(\mathbf{u}^{(i)}, \mathbf{w}^{(i)})$. In the above we recall that, e.g., $\boldsymbol{\varphi}^{(1)}(\mathbf{X}) = \mathbf{X} + \mathbf{u}^{(1)}(\mathbf{X})$ so that $\Delta\boldsymbol{\varphi}^{(1)}(\mathbf{X}) = \Delta\mathbf{u}^{(1)}(\mathbf{X})$. We also see the reactive tractions $\lambda\, \partial g / \partial \mathbf{u}^{(i)}$ acting on $\gamma = \gamma^{(i)}$ which are necessary to enforce the $g = 0$ constraint. For future reference, in the above we define the contact residual r_c and the net residual r.

To derive the tangent for the Newton iterations we note that

$$\delta r(\mathbf{u}, \lambda, \mathbf{w}, \beta; \Delta\mathbf{u}, \Delta\lambda) = \delta r_b(\mathbf{u}, \mathbf{w}; \Delta\mathbf{u}) + \delta r_c(\mathbf{u}, \lambda, \mathbf{w}, \beta; \Delta\mathbf{u}, \Delta\lambda)\,, \tag{12}$$

where

$$\begin{aligned} \delta r_c(\mathbf{u}, \lambda, \mathbf{w}, \beta; \Delta\mathbf{u}, \Delta\lambda) \quad &= \quad \int_{\gamma} \Delta\lambda\, \delta g(\boldsymbol{\varphi}; \mathbf{w})\, \mathrm{d}a \\ &\qquad + \int_{\gamma} \lambda\, \delta^2 g(\boldsymbol{\varphi}; \mathbf{w}; \Delta\mathbf{u})\, \mathrm{d}a \\ &\qquad + \int_{\gamma} \beta\, \delta g(\boldsymbol{\varphi}; \Delta\mathbf{u})\, \mathrm{d}a \\ &\qquad + \int_{\gamma} (\lambda\, \delta g(\boldsymbol{\varphi}; \mathbf{w}) + \beta\, g(\boldsymbol{\varphi}))\, \mathrm{div}_{\gamma} \Delta\mathbf{u}^{(1)} \mathrm{d}a\,, \end{aligned} \tag{13}$$

and div_{γ} denotes the surface divergence operator. Note that $\delta^2 g(\boldsymbol{\varphi}; \mathbf{w}; \Delta\mathbf{u}) = \frac{d}{d\epsilon} \delta g(\boldsymbol{\varphi} + \epsilon\, \Delta\mathbf{u}; \mathbf{w}) \mid_{\epsilon=0}$ is the variation of $\delta g(\boldsymbol{\varphi}; \mathbf{w})$ with respect to $\boldsymbol{\varphi}$ in the direction $\Delta\mathbf{u}$. Having δr we can perform Newton iterations for the LMM by solving $r + \delta r = 0$ for the increment $(\Delta\mathbf{u}, \Delta\lambda)$ and updating $(\mathbf{u}, \lambda) \leftarrow (\mathbf{u}, \lambda) + (\Delta\mathbf{u}, \Delta\lambda)$. Before proceeding to the next Newton iteration, the active set should be updated appropriately. Line search is used within each Newton iteration to increase robustness.

4. Sensitivity analysis

Efficient sensitivity analysis is absolutely necessary for computationally viable design optimization. In this section we present our adjoint sensitivity formulation. We discuss computational aspects in the following section.

---

[3] It can be shown to approach the exact derivative as the mesh is refined

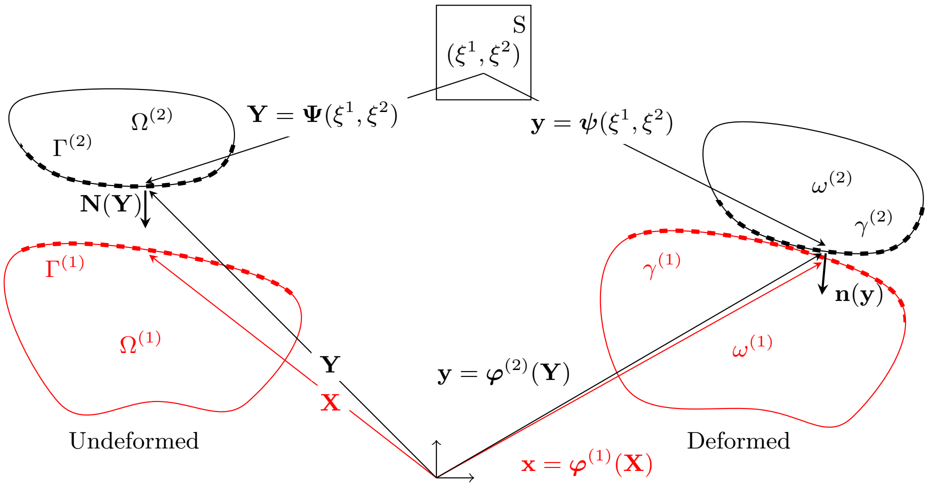

Figure 1: Contacting bodies in (left) undeformed and (right) deformed configurations. Red and black dashed lines denote the slave and master (left) undeformed and (right) deformed surfaces.

For our design sensitivity analysis we consider variations of a general response function with respect to the volume fraction ν which serves as the design field in the optimization problem. Notably the stress $\mathbf{P}(\mathbf{F}, \nu)$ has both explicit dependence on ν as well as implicit dependence due to $\mathbf{F}$. The response function we consider is

$$\theta(\nu) = \sum_{i=1}^{2} \int_{\Omega^{(i)}} \pi(\mathbf{u}^{(i)}, \nabla \mathbf{u}^{(i)}, \nu)\, \mathrm{d}V + \int_{\gamma} \zeta\,(\lambda)\; \mathrm{d}a\,. \tag{14}$$

Note that this functional incorporates the contact pressure which allows us to design for meaningful contact responses, e.g., total contact force or contact force uniformity. The variation, i.e., sensitivity, of the above is

$$\delta_\nu \theta = \sum_{i=1}^{2} \int_{\Omega^{(i)}} (\nabla_1 \pi \cdot \delta_\nu \mathbf{u}^{(i)} + \nabla_2 \pi \cdot \nabla \delta_\nu \mathbf{u}^{(i)} + \nabla_3 \pi\, \delta\nu)\, \mathrm{d}V + \int_\gamma \zeta' \delta_\nu \lambda \, \mathrm{d}a + \int_\gamma \zeta \, \mathrm{div}_\gamma \delta_\nu \mathbf{u}^{(1)} \mathrm{d}a\,, \tag{15}$$

where, e.g., $\delta_\nu \mathbf{u}^{(i)}(\nu; \delta\nu) = \frac{d}{d\epsilon} \mathbf{u}(\nu + \epsilon\, \delta\nu)\,|_{\epsilon=0}$ is the variation of the displacement at ν with respect to $\delta\nu$.

To derive an expression for the sensitivity we use the adjoint method whereby we take the variation of Equation (11) with respect to ν to obtain the identity

$$\begin{aligned} \delta_\nu r(\mathbf{u}, \lambda, \mathbf{w}, \beta; \delta\nu) = 0 \quad &= \quad \delta r_b(\mathbf{u}, \mathbf{w}; \delta_\nu \mathbf{u}) + \sum_{i=1}^{2} \int_{\Omega^{(i)}} \nabla \mathbf{w}_i \cdot \delta_\nu \mathbf{P}\, \mathrm{d}V + \delta r_c(\mathbf{u}, \lambda, \mathbf{w}, \beta; \delta_\nu \mathbf{u}, \delta_\nu \lambda) \\ &= \quad \delta r(\mathbf{u}, \lambda, \mathbf{w}, \beta; \delta_\nu \mathbf{u}, \delta_\nu \lambda) + \sum_{i=1}^{2} \int_{\Omega^{(i)}} \nabla \mathbf{w}_i \cdot \delta_\nu \mathbf{P}\, \mathrm{d}V\,, \end{aligned} \tag{16}$$

where $\delta_\nu \mathbf{P}(\mathbf{F}, \nu; \delta\nu)$ is the variation of $\mathbf{P}$ at $(\mathbf{F}, \nu)$ with respect to ν in the direction of $\delta\nu$, i.e., $\mathbf{F}$ is fixed.

Subtracting the above zero quantity from $\delta_\nu\theta$ gives

$$\begin{aligned}\delta_\nu\theta &= \sum_{i=1}^{2}\int_{\Omega^{(i)}}(\nabla_1\pi\cdot\delta_\nu\mathbf{u}^{(i)}+\nabla_2\pi\cdot\nabla\delta_\nu\mathbf{u}^{(i)}+\nabla_3\pi\,\delta\nu)\,\mathrm{d}V+\int_\gamma\zeta'\delta_\nu\lambda\,\mathrm{d}a+\int_\gamma\zeta\,\mathrm{div}_\gamma\delta_\nu\mathbf{u}\mathrm{d}a\\ &\quad-\delta_\nu r(\mathbf{u},\lambda,\mathbf{w},\beta;\delta\nu)\,.\end{aligned}\tag{17}$$

Rearranging the above we obtain

$$\begin{aligned}\delta_\nu\theta &= \sum_{i=1}^{2}\int_{\Omega^{(i)}}(\nabla_3\pi\,\delta\nu-\nabla\mathbf{w}^{(i)}\cdot\delta_\nu\mathbf{P})\,\mathrm{d}V \qquad (18)\\ &\quad-\Bigg\{\delta r(\mathbf{u},\lambda,\mathbf{w},\beta;\delta_\nu\mathbf{u},\delta_\nu\lambda)-\sum_{i=1}^{2}\int_{\Omega^{(i)}}\left(\nabla_1\pi\cdot\delta_\nu\mathbf{u}^{(i)}+\nabla_2\pi\cdot\nabla\delta_\nu\mathbf{u}^{(i)}\right)\mathrm{d}V\\ &\quad-\int_\gamma\zeta'\delta_\nu\lambda\,\mathrm{d}a-\int_\gamma\zeta\,\mathrm{div}_\gamma\delta_\nu\mathbf{u}^{(1)}\mathrm{d}a\Bigg\}\,.\end{aligned}$$

We can annihilate the term in braces which contains the implicitly defined variations $\delta_\nu\mathbf{u}^{(i)}$ and $\delta_\nu\lambda$ by requiring the heretofore arbitrary $\mathbf{w}^{(i)}\in\mathcal{W}_0$ and $\beta\in L^2$ to satisfy

$$\begin{aligned}\delta r(\mathbf{u},\lambda,\mathbf{w},\beta;\delta_\nu\mathbf{u},\delta_\nu\lambda) &= \sum_{i=1}^{2}\int_{\Omega^{(i)}}\left(\nabla_1\pi\cdot\delta_\nu\mathbf{u}^{(i)}+\nabla_2\pi\cdot\nabla\delta_\nu\mathbf{u}^{(i)}\right)\mathrm{d}V\\ &\quad+\int_\gamma\zeta'\delta_\nu\lambda\,\mathrm{d}a+\int_\gamma\zeta\,\mathrm{div}_\gamma\delta_\nu\mathbf{u}^{(1)}\mathrm{d}a\end{aligned}\tag{19}$$

for all $\delta_\nu\mathbf{u}^{(i)}\in\mathcal{W}_0$ and $\delta_\nu\lambda\in L^2$. Note that δr is the same variation that is used in the Newton iteration, cf. Equation (12) so it is readily available. For more insight of this adjoint problem, we expand Equation (19)

$$\begin{aligned}&\delta r_b(\mathbf{u},\mathbf{w};\delta_\nu\mathbf{u})+\int_\gamma\left(\beta\,\delta g(\boldsymbol{\varphi};\delta_\nu\mathbf{u})+\beta\,g(\boldsymbol{\varphi})\,\mathrm{div}_\gamma\delta_\nu\mathbf{u}^{(1)}\right)\mathrm{d}a\\ &+\int_\gamma\lambda\,\delta^2 g(\boldsymbol{\varphi};\mathbf{w};\delta_\nu\mathbf{u})\,\mathrm{d}a+\int_\gamma\lambda\,\delta g(\boldsymbol{\varphi};\mathbf{w})\,\mathrm{div}_\gamma\delta_\nu\mathbf{u}^{(1)}\mathrm{d}a\\ &+\int_\gamma\delta_\nu\lambda\,\overbrace{(\delta g(\boldsymbol{\varphi};\mathbf{w})\;-\zeta')}^{g_{adj}}\,\mathrm{d}a\\ &=\sum_{i=1}^{2}\int_{\Omega^{(i)}}\left(\nabla_1\pi\cdot\delta_\nu\mathbf{u}^{(i)}+\nabla_2\pi\cdot\nabla\delta_\nu\mathbf{u}^{(i)}\right)\mathrm{d}V+\int_\gamma\zeta\,\mathrm{div}_\gamma\delta_\nu\mathbf{u}^{(1)}\mathrm{d}a\,,\end{aligned}\tag{20}$$

to see that 1) $\nabla_1\pi$ and $\nabla_2\pi$ act as a body load and an initial stress in the adjoint problem, 2) $\beta\,\delta g(\boldsymbol{\varphi};\delta_\nu\mathbf{u})+\cancelto{0}{\beta\,g(\boldsymbol{\varphi})}\mathrm{div}_\gamma\delta\mathbf{u}^{(1)}$ is the source of the adjoint reactive traction that enforces the *linear* adjoint contact constraint $g_{adj}=\delta g(\boldsymbol{\varphi};\mathbf{w})-\zeta'=0$ on $\mathbf{w}^{(1)}$ and $\mathbf{w}^{(2)}$ over γ, 3) this adjoint constraint involves only bilateral constraints, i.e., there is no analogue to Equation (9), so β is interpreted as the adjoint Lagrange multiplier which can take both positive and negative values, 4) $\zeta\mathrm{div}_\gamma\delta_\nu\mathbf{u}^{(1)}$ corresponds to an adjoint surface load, 5) $\int_\gamma\lambda\,\delta^2 g(\boldsymbol{\varphi};\mathbf{w};\delta_\nu\mathbf{u})\,\mathrm{d}a+\int_\gamma\lambda\,\delta g(\boldsymbol{\varphi};\mathbf{w})\,\mathrm{div}_\gamma\delta_\nu\mathbf{u}^{(1)}\mathrm{d}a$ is an additional adjoint contact induced stiffness over γ.

Upon solving the adjoint problem (19), the sensitivity reduces to

$$\delta_\nu \theta = \sum_{i=1}^{2} \int_{\Omega^{(i)}} (\nabla_3 \pi \, \delta\nu - \nabla \mathbf{w}^{(i)} \cdot \delta_\nu \mathbf{P}) \, \mathrm{d}V \, . \tag{21}$$

5. Solution algorithms

We can directly solve the above primal and adjoint saddle point problems of Equations (11) and (19). Alternatively we can solve them via the penalty or augmented Lagrangian methods.

5.1. Penalty Method

In the PM we no longer have a constraint, per se. Rather for the primal analysis we define r as

$$r(\mathbf{u}, \mathbf{w}) \;\; = \;\; r_b(\mathbf{u}, \mathbf{w}) + \int_\gamma \tilde{\lambda} \, \delta g(\boldsymbol{\varphi}; \mathbf{w}) \, \mathrm{d}a \, , \tag{22}$$

where

$$\tilde{\lambda} = \sum_{A=1}^{\mathcal{N}_c} N_A^{(1)}(\boldsymbol{\varphi}^{(1)}) \, \epsilon \langle \mathrm{g}_A \rangle \, , \tag{23}$$

ϵ is a fixed penalty parameter, and to consider only active constraints we invoke the Macauley bracket $\langle \, \rangle$ representing the ramp function, i.e., $\langle g \rangle = g$ if $g > 0$, and $\langle g \rangle = 0$ if $g \leq 0$. Note that we replace the nodal Lagrange multipliers λ_A with the penalized gaps such $\lambda_A \approx \epsilon \, \langle \mathrm{g}_A \rangle$, cf. Equations (7b) and 8.

We use Newton's method to evaluate the $\mathbf{u}^{(i)}$ that solves Equation (11) with the r of Equation (22). For completeness we note that

$$\begin{aligned} \delta r(\mathbf{u}, \mathbf{w}; \Delta\mathbf{u}) \;\; = \;\; & \delta r_b(\mathbf{u}, \mathbf{w}; \Delta\mathbf{u}) \\ & + \int_\gamma \Delta\tilde{\lambda} \, \delta g(\boldsymbol{\varphi}; \mathbf{w}) \, \mathrm{d}a \\ & + \int_\gamma \tilde{\lambda} \, \delta^2 g(\boldsymbol{\varphi}; \mathbf{w}; \Delta\mathbf{u}) \, \mathrm{d}a \\ & + \int_\gamma \tilde{\lambda} \, \delta g(\boldsymbol{\varphi}; \mathbf{w}) \, \mathrm{div}_\gamma \Delta\mathbf{u}^{(1)} \, \mathrm{d}a \, , \end{aligned} \tag{24}$$

where

$$\Delta\tilde{\lambda} = \sum_{A=1}^{\mathcal{N}_c} N_A^{(1)}(\boldsymbol{\varphi}^{(1)}) \, \epsilon \, H(\mathrm{g}_A) \; \Delta \mathrm{g}_A \, (\boldsymbol{\varphi}; \Delta\mathbf{u}) \; , \tag{25}$$

and H is the Heaviside function, i.e., $H(g) = 1$ if $g > 0$ and $H(g) = 0$ if $g < 0$.

This approach poses no conceptual difficulty to the usual unconstrained sensitivity analysis, i.e., we merely "turn the crank." Specifically, we solve the adjoint problem of Equation (19) with the δr of Equation (24) for $\mathbf{w}^{(i)}$ and then evaluate the sensitivity of Equation (21).

5.2. Augmented Lagrangian Method

In the ALM, $\mathbf{u}^{(i)}$ and λ are both evaluated, but they are not solved as a coupled problem via Newton's method. First a guess is taken for the nodal Lagrange multipliers λ_A and subsequently used to define the residual Equation (22) where

$$\tilde{\lambda} = \sum_{A=1}^{\mathcal{N}_c} N_A^{(1)}(\boldsymbol{\varphi}^{(1)}) \; \langle \lambda_A + \epsilon \, \mathrm{g}_A \rangle \; , \tag{26}$$

and again ϵ is a fixed penalty parameter. We then apply Newton's method to solve Equation (22) for the $\mathbf{u}^{(i)}$. Using this $\mathbf{u}^{(i)}$ we update the nodal Lagrange multipliers

$$\lambda_A \leftarrow \langle \lambda_A + \epsilon \, g_A \rangle \ . \tag{27}$$

The procedure of evaluating $\mathbf{u}^{(i)}$ and updating $\tilde{\lambda}$ is repeated until convergence. And again for completeness we note that the tangent operator is given again by Equation (24) where

$$\Delta\tilde{\lambda} = \sum_{A=1}^{\mathcal{N}_c} N_A^{(1)}(\boldsymbol{\varphi}^{(1)}) \, H\left(\lambda_A + \epsilon \, g_A\right) \epsilon \ \ \Delta g_A\left(\boldsymbol{\varphi}; \Delta\mathbf{u}\right) \ . \tag{28}$$

After convergence, Equation (11) is satisfied so no change is necessary for our adjoint sensitivity formulation. However, if one is using the ALM to solve the primal problem it also makes sense to use it to solve the adjoint problem. As such we solve the adjoint problem of Equation (19) by guessing a β and then finding $\mathbf{w}^{(i)} \in \mathcal{W}_0$. To do this, we use the same finite element discretization of the primal analysis, so $\mathbf{w}$ is the adjoint displacement and β is the adjoint Lagrange multiplier.

To reuse terms of the primal analysis, we compute the nodal adjoint constraint as

$$g_A^{adj} = \delta g_A\left(\boldsymbol{\varphi}; \mathbf{w}\right) - \frac{\partial\theta}{\partial\lambda_A} \, . \tag{29}$$

We also replace β_A with $H(\lambda_A)\left(\beta_A + \epsilon \, g_A^{adj}\right)$ in the integral $\int_\gamma \beta \, \delta g(\boldsymbol{\varphi}; \delta_\nu \mathbf{u}) \, \mathrm{d}a = \sum_{A=1}^{\mathcal{N}_c} \beta_A \, \delta g_A(\boldsymbol{\varphi}; \delta_\nu \mathbf{u})$ that appears in Equation (20). Specifically, this integral $\int_\gamma \beta \, \delta g(\boldsymbol{\varphi}; \delta_\nu \mathbf{u}) \, \mathrm{d}a$ is replaced by the following equation

$$\begin{aligned}
&\sum_{A=1}^{\mathcal{N}_c} H(\lambda_A) \left(\beta_A + \epsilon \ g_A^{adj}\right) \ \delta g_A(\boldsymbol{\varphi}; \delta_\nu \mathbf{u}) \\
&\qquad = \sum_{A=1}^{\mathcal{N}_c} H(\lambda_A) \left(\beta_A - \epsilon \frac{\partial\theta}{\partial\lambda_A}\right) \int_\gamma N_A^{(1)}(\boldsymbol{\varphi}^{(1)}) \, \delta g(\boldsymbol{\varphi}; \delta_\nu \mathbf{u}) \mathrm{d}a \\
&\qquad\quad + \sum_{A=1}^{\mathcal{N}_c} H(\lambda_A) \, \epsilon \ \left(\int_\gamma N_A^{(1)}(\boldsymbol{\varphi}^{(1)}) \, \delta g\left(\boldsymbol{\varphi}; \mathbf{w}\right) \ \mathrm{d}a\right) \ \delta g_A(\boldsymbol{\varphi}; \delta_\nu \mathbf{u}) \\
&\qquad = \int_\gamma \beta^* \ \delta g(\boldsymbol{\varphi}; \delta_\nu \mathbf{u}) \mathrm{d}a + \int_\gamma \delta\tilde{\lambda} \, \delta g\left(\boldsymbol{\varphi}; \mathbf{w}\right) \ \mathrm{d}a \, ,
\end{aligned} \tag{30}$$

where $\beta^* = \sum_{A=1}^{\mathcal{N}_c} H(\lambda_A) \left(\beta_A - \epsilon \frac{\partial\theta}{\partial\lambda_A}\right) \ N_A^{(1)}(\boldsymbol{\varphi}^{(1)})$ and $\delta\tilde{\lambda} = \sum_{A=1}^{\mathcal{N}_c} N_A^{(1)}(\boldsymbol{\varphi}^{(1)}) \, H\left(\lambda_A\right) \epsilon \ \ \delta g_A\left(\boldsymbol{\varphi}; \delta_\nu \mathbf{u}\right)$. Consequently Equation (20), i.e., the adjoint problem, requires that we find $\mathbf{w} \in \mathcal{W}_0$ such that

$$
\begin{aligned}
& \delta r_b(\mathbf{u}, \mathbf{w}; \delta_\nu \mathbf{u}) \\
& + \int_\gamma \delta\tilde{\lambda}\, \delta g(\boldsymbol{\varphi}; \mathbf{w})\, \mathrm{d}a \\
& + \int_\gamma \tilde{\lambda}\, \delta^2 g(\boldsymbol{\varphi}; \mathbf{w}; \delta_\nu \mathbf{u})\, \mathrm{d}a + \\
& + \int_\gamma \tilde{\lambda}\, \delta g(\boldsymbol{\varphi}; \mathbf{w})\, \mathrm{div}_\gamma \delta \mathbf{u}^{(1)}\, \mathrm{d}a \\
= \; & \sum_{i=1}^{2} \int_{\Omega^{(i)}} \left(\nabla_1 \pi \cdot \delta_\nu \mathbf{u}^{(i)} + \nabla_2 \pi \cdot \nabla \delta_\nu \mathbf{u}^{(i)} \right) \mathrm{d}V \\
& - \int_\gamma \beta^*\, \delta g(\boldsymbol{\varphi}, \delta_\nu \mathbf{u})\, \mathrm{d}a \\
& + \int_\gamma \zeta\, \mathrm{div}_\gamma \delta_\nu \mathbf{u}^{(1)} \mathrm{d}a - \int_\gamma \cancelto{0}{\beta g}\, \mathrm{div}_\gamma \delta_\nu \mathbf{u}^{(1)} \mathrm{d}a
\end{aligned}
\tag{31}
$$

for all $\delta_\nu \mathbf{u}^{(i)} \in \mathcal{W}_0$. Using this $\mathbf{w}^{(i)}$ we update

$$
\beta_A \leftarrow H(\lambda_A) \left(\beta_A + \epsilon\, \mathsf{g}_A^{adj} \right) . \tag{32}
$$

The procedure of solving the *linear* problem of Equation (31) for $\mathbf{w}^{(i)}$ and updating β is repeated until convergence whereupon we compute the sensitivity of Equation (21).

Note that we have to iterate here to solve the linear adjoint problem. However, this may be a desirable means to solve the saddle point problem, especially since the convergence is global and super linear [55]. Also note that the primal bilinear operator $\delta r(\mathbf{u}, \mathbf{w}; \Delta \mathbf{u})$ of Equation (24) that appears in the Newton iteration for $\Delta \mathbf{u}^{(i)}$ does equal the adjoint bilinear operator, i.e., the left hand side of Equation (31), that appears in the computation for $\mathbf{w}^{(i)}$ upon convergence of the primal problem. So the adjoint tangent stifness matrix is equivalent to the converged tangent stiffness matrix of the primal analysis. Further note that in the primal ALM analysis the tangent matrix changes with each Lagrange multiplier update. This is not the case in the adjoint ALM analysis, which uses a fixed tangent matrix and constraint active set, taken from the converged primal analysis, for all the adjoint Lagrange multipliers updates. When using direct solvers, this matrix is already available in factored form. It would also be possible to further reduce the system by a Schur reduction to only contact degrees-of-freedom, as in [56], further reducing the cost of each augmentation, though with additional upfront cost and complexity. Finally we note that we must subtract the integral $\int_\gamma \beta^*\, \delta g(\boldsymbol{\varphi}; \delta_\nu \mathbf{u})\, \mathrm{d}a$, cf. Equation (31), in the adjoint load linear term. Fortunately this integral is similar to the $\int_\gamma \tilde{\lambda}\, \delta g(\boldsymbol{\varphi}; \mathbf{w})\, \mathrm{d}a$ integral that appears in the primal analysis residual Equation (22). The adjoint load has two additional terms $\int_\gamma \zeta\, \mathrm{div}_\gamma \delta_\nu \mathbf{u}^{(1)} \mathrm{d}a$ and $-\int_\gamma \beta\, g\, \mathrm{div}_\gamma \delta_\nu \mathbf{u}^{(1)} \mathrm{d}a$ where the latter is zero upon convergence since again β is zero where the constraint is inactive, i.e., $\beta_A \mathsf{g}_A = 0$.

The finite element analysis of the adjoint problem using the ALM is summarized in Algorithm 1. The adjoint load, i.e., right hand side of Equation (31), is discretized as $\delta_\nu \mathbf{U}^\top \mathbf{F}^{adj}$. We solve the linear adjoint problem with the same tangent stiffness matrix $\mathbf{K}$ which is derived from the δr of Equation (24) of the ALM primal problem. This process is repeated until the norm of the adjoint constraint is satisfied to within a user-defined tolerance, i.e., $|\mathbf{G}^{adj}| < \epsilon_{adj}$ where $\mathbf{G}^{adj} = [\mathsf{g}_1^{adj}, \mathsf{g}_2^{adj}, \ldots, \mathsf{g}_{\mathcal{N}_c}^{adj}]^\top$.

As discussed on numerous occasions, non-differentiability occurs in cases of strict complementary, i.e., $\lambda_A = 0$ and $\mathsf{g}_A = 0$. We assume this case is rare in practical computations. Nevertheless, in our algorithm, if a node has zero pressure, i.e., $\lambda_A = 0$, it is treated as an inactive constraint. For validation, we compare our computed sensitivities with the sensitivities obtained by finite differences. These computations agree to within small discrepancies that are attributed to the truncation and round–off errors of the finite difference

Algorithm 1: Adjoint sensitivity analysis for ALM

```
compute $\theta$, $\partial\theta/\partial\mathbf{U}$, $\partial\theta/\partial\boldsymbol{\Lambda}$ ;
initialize $\mathbf{W}^0$ and $\boldsymbol{\beta}^0$ to zero;
do
    compute $\mathbf{G}^{adj}$;
    update $\beta_A \leftarrow H(\lambda_A)\left(\beta_A + \epsilon\, g_A^{adj}\right)$ ;
    solve $\mathbf{K}^\top\mathbf{W}^{j+1} = \mathbf{F}^{adj}$ for $\mathbf{W}^{j+1}$ ;
while $|\mathbf{G}^{adj}| > \epsilon_{adj}$;
```

computation. We attribute this accuracy to the use of the mortar segment-to-segment method principally because if a new node is introduced to the active set of the contact surface there is a smooth variation of the contact forces.

6. Optimization problem

In the usual topology optimization strategy known as the density method, the design domain Ω_d is defined by piecewise uniform element volume fraction field which equals ν_e over each element Ω_e of the finite element mesh over the hold-all domain Ω such that $\Omega_d = \bigcup_{e \,\ni\, \nu_e = 1} \Omega_e$. In this representation, designs do not converge as the mesh is refined. It is well known that more holes appear as the mesh is refined, and 'checker board' patterns appear. Consequently, this representation requires length scale control to define a well-posed topology optimization problem [57, 58]. Several such controls have been proposed in the literature, e.g., filtering, perimeter constraint, and slope constraint. For instance, in the filtering approach [57], a smoothed volume fraction $\tilde{\nu}$ replaces the ν in the previous equations. The smoothing is obtained through a filter such that

$$\hat{\nu}(\mathbf{X}) = \int_{B_r(\mathbf{X})} k(|\mathbf{Y} - \mathbf{X}|)\, \nu(\mathbf{Y})\, \mathrm{d}V\,, \tag{33}$$

where k is a suitable kernel function and $B_r(\mathbf{X})$ is a ball of radius r centered at $\mathbf{X}$. For the computations we use an element-wise uniform parameterizations for ν and $\hat{\nu}$; the latter are evaluated at the element centroids $\mathbf{X}_i$ using a one-point quadrature to approximate the integral $\hat{\nu}(\mathbf{X}_i) = \int_{B_r(\mathbf{X})} k(|\mathbf{Y} - \mathbf{X}_i|)\, \nu(\mathbf{Y})\, \mathrm{d}V$. Ultimately, we obtain the relation $\hat{\boldsymbol{\nu}} = \mathbf{G}\mathbf{d}$ where $G_{ij} = k(\mathbf{X}_i - \mathbf{X}_j)|\Omega_j|$ if $|\mathbf{X}_i - \mathbf{X}_j| \leq r$ otherwise $G_{ij} = 0$, $|\Omega_j|$ is the volume of the element Ω_j, and $\mathbf{d} = \boldsymbol{\nu}$ is the design variable vector, i.e. element volume fractions.

An alternative to these length scale control techniques is to use a design parameterization that is independent to the finite element mesh and that also enforces length scale control. In our work, we define Ω_d using an implicit function ϕ via the level-set method, i.e., $\Omega_d = \{\mathbf{X} \in \Omega \,|\, \phi(\mathbf{X}) \geq 0\}$. This level-set representation allows us to do shape, material, and topology optimization [59]. For the optimization, we parameterize ϕ, via B-splines [52] such that we now have

$$\phi(\mathbf{X}, \mathbf{d}) = \mathbf{d}^\top \hat{\mathbf{N}}(\mathbf{X})\,, \tag{34}$$

where $\hat{\mathbf{N}}(\mathbf{X}) = [\hat{N}_1(\mathbf{X}), \hat{N}_2(\mathbf{X}), ..., \hat{N}_n(\mathbf{X})]^\top$ is the vector of B-spline basis functions, and $\mathbf{d} = [d_1, d_2, ..., d_n]^\top$ is the vector of control points , i.e. design variables. Now the "height" components d_i of $\mathbf{d}$ replace the element volume fraction parameters $d_i = \nu_i$ as the design variables. In this way, we do not need to introduce other restriction methods, e.g., filters, to formulate a well–posed TO problem. Notably, the cost associated with filtering is replaced by the cost of the B-spline computations which is small since our tri-cubic B-spline is defined over a rectangular cuboid with dimensions h_x, h_y, and h_z in the respective directions, cf. Appendix B. Similar to the density method, for computation we again assume element-wise uniform level-set and volume fraction parameterizations, and similar to the filter we first evaluate $\boldsymbol{\phi} = \mathbf{G}\mathbf{d}$ where $\mathbf{G}$ is a $n_{fea} \times n_d$

matrix such that $G_{ij} = \hat{N}_j(\mathbf{X}_i)$ if j is a local control point for $\mathbf{X}_i$, otherwise $G_{ij} = 0$, where $\mathbf{X}_i$ is the element Ω_i centroid. The computation of $\mathbf{G}$ is straightforward and does not require knowledge of the connectivity between the elements in the finite element mesh. This is specially advantageous for unstructured meshes. Finally, the number of nonzero matrix elements in $\mathbf{G}$ is dictated by the number of local control points n_c per B-spline basis functions and the number of finite elements, i.e., $n_{fea} \times n_c$.

We define the volume fraction via ϕ and the smoothed Heaviside function

$$\begin{aligned} \nu(\mathbf{X}, \mathbf{d}) &= H_\eta(\phi(\mathbf{X}, \mathbf{d})) \\ &= \frac{1}{2} + \frac{1}{2} \tanh\left(\eta\, \phi(\mathbf{X}, \mathbf{d})\right) , \end{aligned} \tag{35}$$

where η governs the smoothness such that H_η approximates the Heaviside as $\eta \to \infty$. Note that the volume fraction is continuous and independent of the finite element mesh. Since we restrict the control points to $d_i \in [-1, 1]$ and use tri-cubic B-splines, the gradient $|\nabla\phi| \leq 27/(8h_x h_y h_z)$ is bounded and hence so is $|\nabla\nu| = H'_\eta(\phi)|\nabla\phi|$. In this way, the B-spline parameterization necessarily enforces a "slope" constraint [60], and prohibits small features, and thus renders a well-posed TO problem as dictated by the values of h_x, h_y, h_z, and η.

In our SIMP/*ersatz* approach, we define

$$\tilde{\nu} = (1 - \nu_0)\, \nu^p + \nu_0 \,, \tag{36}$$

where ν_0 is the "small" lower volume fraction limit and p is the penalty parameter. Using the above, the material response is weighted by $\tilde{\nu}$, i.e.,

$$W^* = \tilde{\nu}\, W \,, \tag{37}$$

$$\mathbf{P}(\mathbf{F}, \tilde{\nu}) = \tilde{\nu}\, \nabla W(\mathbf{F}) \,, \tag{38}$$

$$D\mathbf{P}(\mathbf{F}, \tilde{\nu}) = \tilde{\nu}\, D^2 W(\mathbf{F}) \,, \tag{39}$$

where W is the hyperelastic energy function for the "stiff" material. For details of the hyperelastic energy function used in our examples please refer to Appendix C.

In this erzatz approach, the contact conditions are satisfied for all contact surface regions regardless of their volume fraction. However, if a void region experiences contact, i.e., the gap is zero, the corresponding pressure Lagrange multipliers are small.

Note that the contact, sensitivities, and material model formulation is general, so we can use any parameterization for $\tilde{\nu}$. For comparison purposes, we will use both, the density method of Equation (33) and the B-spline representation of Equation (34) in our examples. To have a fair comparison, the design field has the same lower and upper bounds, i.e., $d : \Omega \to [-1, 1]$, and both methods use the threshold and penalization Equations (35) and (36). For the density method, the element volume fraction is computed by first filtering the element design parameters to obtain the element level set values $\boldsymbol{\phi} = \mathbf{G}\mathbf{d}$ and subsequently the element volume fractions are evaluated via Equations (35) and (36).

Our general topology optimization problem is defined as

$$\begin{aligned} \min_{\mathbf{d}} \quad & f \\ \text{subject to} \quad & g_j \leq 0, \quad j = 1, 2, ..., m \,. \end{aligned} \tag{40}$$

In the examples, we use the following cost functions,

$$
\begin{aligned}
f_a &= -\int_\omega W^* \mathrm{d}v \,, && (41)\\
f_b &= \sum_{i=1}^{2} \left[\int_{\Omega^{(i)}} \mathbf{u}^{(i)} \cdot \mathbf{b}^{(i)} \, \nu \, \mathrm{d}V + \int_{A^{t\,(i)}} \mathbf{u}^{(i)} \cdot \mathbf{s}^{p\,(i)} \, \mathrm{d}A \right] , && (42)\\
f_c &= -\int_\gamma \lambda \, \mathrm{d}a \,, && (43)
\end{aligned}
$$

where f_a is the negative of the strain energy, f_b the compliance, and f_c the negative of the total contact force (cf. Appendix A). The negative signs in Equations (41) and (43) imply that we are maximizing the strain energy and maximizing the total contact force.

For the constraint, we use the usual total volume fraction constraint wherein

$$
g_1 = \frac{1}{|\Omega|} \int_\Omega \nu \, \mathrm{d}V - \nu_{max} \,. \tag{44}
$$

7. Examples

In the following subsections, we generate optimal topologies applying the presented method. All the structures are modeled using the neo-Hookean hyperelastic material [61] described in Appendix C. We specify the Young's modulus E and Poisson's ratio v so that the shear and bulk moduli are $\mu = E/(2(1+\mathsf{v}))$ and $\kappa = E/(3(1-2\mathsf{v}))$. We use the finite element software NIKE3D [62] for the finite element simulation since it has contact analysis capabilities. The finite element simulations use (8-noded) tri-linear hexahedral elements and the NIKE3D ALM and mortar segment-to-segment methods [8] to enforce the contact constraints with the ALM penalty parameter $\epsilon = 10$. We model the level-set function with tri-cubic B-splines, cf. Appendix B. The SIMP penalization power is $p = 3$, the lower limit for the penalized volume fraction is $\nu_0 = 10^{-2}$ and the Heaviside parameter is $\eta = 10$. We employ the nonlinear programming software IPOPT [63] to solve the optimization problems. IPOPT converges successfully if the norm of the Karush-Kuhn-Tucker (KKT) optimality conditions is smaller than the tolerance $\epsilon_{\text{opt}} = 10^{-3}$ (cf. Equations (5) and (6) in [63]), unless otherwise stated.

7.1. Cylindrical die pressed into a rectangular domain

In this example, a stiff cylindrical die with Young's modulus $E = 1000$ and Poisson's ratio $\mathsf{v} = 0.3$ is pressed into a compliant rectangular slab with $E = 1$ and $\mathsf{v} = 0.3$ that is fixed at its bottom surface, cf. Figure 2. The die is initially resting on top of the slab before its contact lines displaces -0.6 units in the vertical, i.e., z direction, cf. Figure 3. $12 \times 8 \times 1$ and $23 \times 10 \times 8$ finite element meshes are used to model the die and the slab. The slab serves as the hold-all domain Ω in which we optimize the material distribution to define Ω_d so as to minimize $f_a/|f_a^0|$, i.e., maximize the strain energy, subject to a maximum volume constraint $\nu_{max} = 0.4$ where the nominal, i.e., full volume, strain energy of the slab is $|f_a^0| = 5.014 \times 10^{-2}$.

For comparison purposes, we solve this TO problem with the B-spline parameterization and the more common element-wise parameterization density method. In the latter, every finite element has its own volume fraction parameter ν_e rendering $1840 = 23 \times 10 \times 8$ design variables. The length scale control on the element-wise problem is obtained via filtration with a cone filter radius of $r_f = 0.7$ units [57]. Figure 4a illustrates the optimized filtered volume fractions $\tilde{\nu}_e$ wherein white, gray, and black represent void, porous, and solid material regions respectively. For the B-spline optimization, we model the level-set function ϕ using tri-linear B-splines via $728 = 13 \times 8 \times 7$ control points, i.e., design variables, which corresponds to $h_x = 0.9$, $h_y = 0.8$, and $h_z = 0.75$. The optimal design for this case, cf. Figure 4b, exhibits a smooth well-defined boundary. We repeat this problem for a finer slab element mesh, cf. Figure 5, containing $13500 = 45 \times 20 \times 15$ finite elements. The results are summarized in Table 1 where It., n_d, and n_{fea} refer to the number of optimization iterations, the number of design variables, and the number of finite elements.

For a coarse mesh, the number of iterations for the density method and the B-spline approach are similar (15 and 19, respectively). However, for the refined mesh case, the B-spline approach maintains a similar number of iterations (13) whereas the density approach requires significantly more (41) and in addition the number of filter matrix elements is surprisingly large. We attribute the difference in computational cost to the additional nonlinearities in the design via the cubic nature of the splines. However for the refined mesh, the B-spline design uses less number of design variables compared to the density method resulting in a better efficiency. We also note that the filter and B-spline length scales are controlled in different manners, although we selected the filter radius and B-spline grid so as to obtain similar designs. The difference in feature resolution between these two methods might account for the slightly better design performance obtained by the B-spline method in this case.

The number of nonzero filter matrix elements in $\mathbf{G}$ is small for the density method with coarse mesh. As a result, we notice a few gray elements, cf. Figure 4a. Ideally there would be no gray elements as they indicate regions partially filled with material which we do not allow. As expected, as we refine the mesh and maintain the same filter size the number of nonzero filter matrix elements increases and hence more gray elements appear (albeit they are smaller). As mentioned before, the B-spline parameterization can also be obtained via a $\mathbf{G}$ "filter" matrix. For our tri-cubic B-spline parameterization, the number of nonzero $\mathbf{G}$ matrix elements is given by the number of control points per B-spline basis function and the number of finite elements, i.e., $n_{fea} \times 64$.

In this example, every primal analysis requires 6 loading steps which collectively require 100 Newton iterations and 18 pressure Lagrange multipliers updates, cf. Equation (27). On the other hand, the adjoint analyses requires 5 linear solutions for the Lagrange multipliers updates. Furthermore, the adjoint solution reuses the tangent stiffness matrix from the converged primal analysis so as expected, the computational cost for the adjoint analysis is far smaller than the primal analysis.

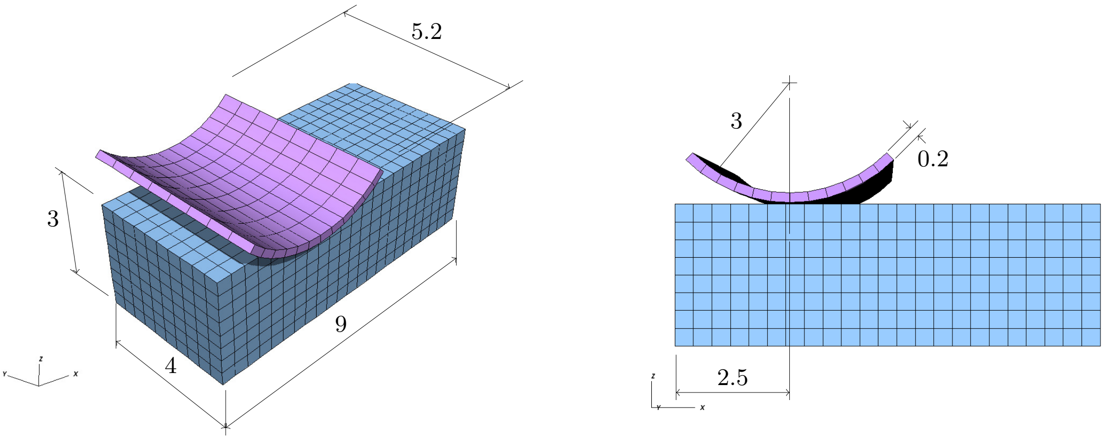

(a) (b)

Figure 2: Cylindrical die pressed into design domain (a) isometric and (b) lateral view.

We now study the effect of the Heaviside function wherein we solve the previous problem over the fine mesh with different parameters $\eta = 4, 6, 8, 10, 12$ for the B-spline approach, cf. Table 2. Figure 6 shows the optimal designs' isosurfaces corresponding to volume fractions $\nu = 0.1$ in green and $\nu = 0.9$ in red. The region between these two surfaces contains the gray, i.e., porous material; it shrinks as η increases. Additionally, the designs with larger η values have better performance (more optimal f_a) as smaller features are permitted. However, a very large η causes numerical issues as the accuracy of the sensitivity computations erode. Indeed, in the extreme case whereby we replace Equation (35) with the Heaviside, we obtain zero sensitivities at all integration points save those on the boundary and at those points the derivative contains the Dirac delta function.

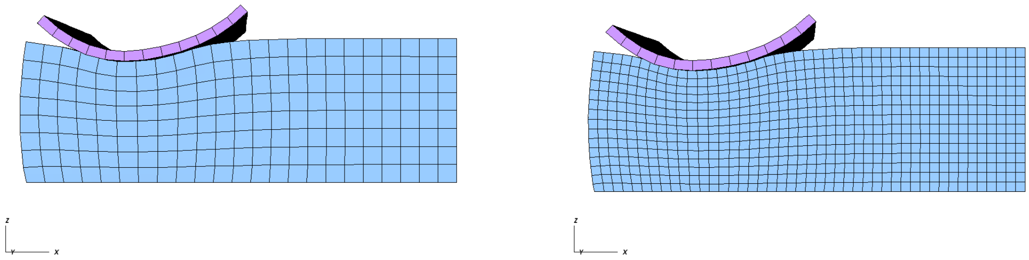

(a) (b)

Figure 3: (a) Deformed configuration for the cylindrical die pressed into design domain (b) using a refined mesh.

Table 1: Optimal design summary for cylindrical die problem.

Method	$f_a/\lvert f_a^0\rvert$	It.	r_f	# nonzero filter matrix elements	n_d	n_{fea}
Density	-0.9889	41	0.7	2 009 512	$13500 = 45 \times 20 \times 15$	$13500 = 45 \times 20 \times 15$
Density	-0.9819	15	0.7	41 272	$1840 = 23 \times 10 \times 8$	$1840 = 23 \times 10 \times 8$
B-spline	-0.9939	13	-	864 000	$728 = 13 \times 8 \times 7$	$13500 = 45 \times 20 \times 15$
B-spline	-0.9908	19	-	117 760	$728 = 13 \times 8 \times 7$	$1840 = 23 \times 10 \times 8$

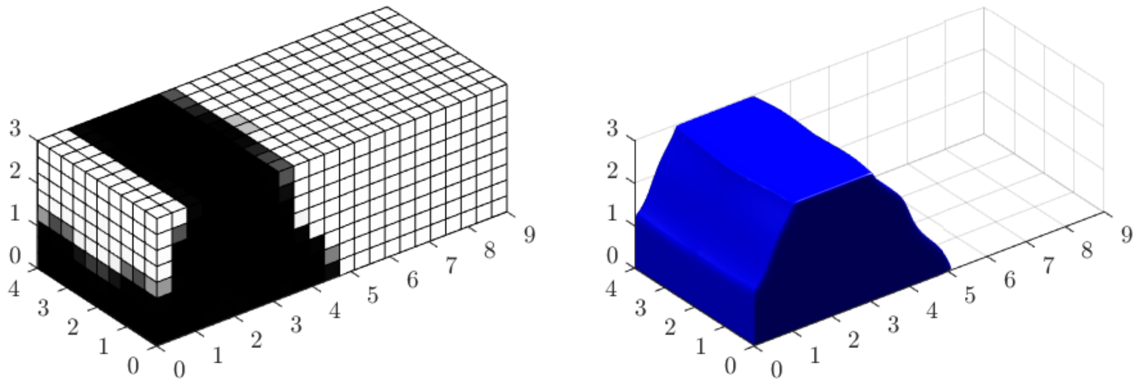

(a) (b)

Figure 4: Optimal topology designs (a) filtered volume fraction (b) B-spline zero-level set for the cylindrical die problem.

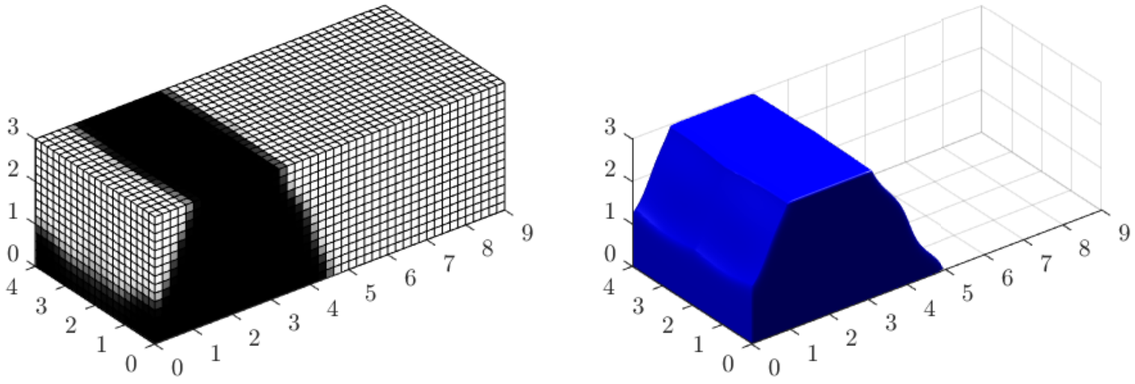

(a) (b)

Figure 5: Optimal topology designs (a) filtered volume fraction (b) B-spline zero-level set for the cylindrical die problem using a refined mesh.

It is worth noting that the optimizer mainly updates the gray regions because of their nonzero gradients, cf. Equation (35). And since the gray region is penalized by the SIMP, the optimizer places material judiciously, reducing the extent of gray region and thereby generating a predominantly black/white design. For this reason, our initial design is totally gray, i.e., $d_i = \log(\nu_{max}/(1-\nu_{max}))/2\eta$, which reduces the initial design dependency and satisfies the volume fraction constraint.

Table 2: Optimal design summary for cylindrical die problem corresponding to different η.

$f_a/\lvert f_a^0\rvert$	It.	η
-0.9778	13	4
-0.9892	11	6
-0.9904	21	8
-0.9939	13	10
-0.9958	14	12

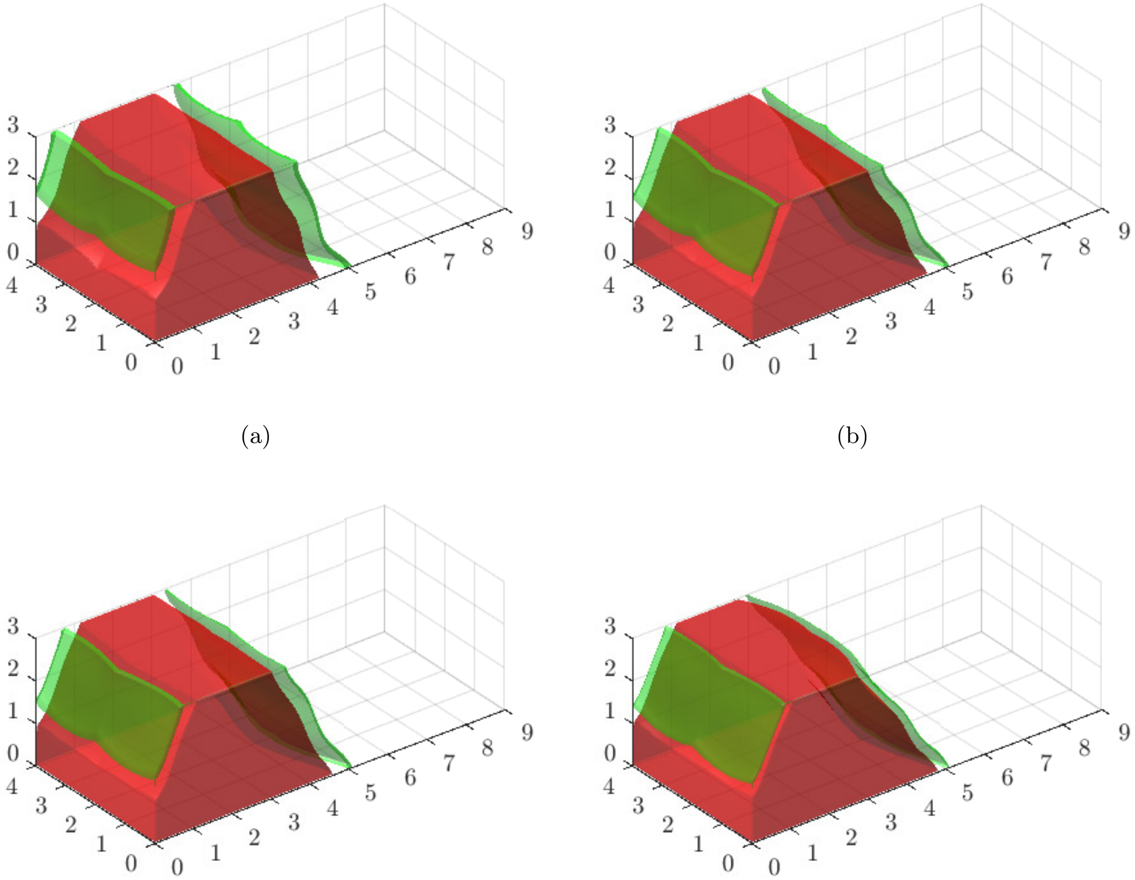

(a)

(b)

(c)

(d)

Figure 6: Optimal topology designs' isosurfaces corresponding to volume fractions $\nu = 0.1$ in green and $\nu = 0.9$ in red for the cylindrical die problem with B-spline approach (a) $\eta = 4$, (b) $\eta = 6$, (c) $\eta = 8$, and (d) $\eta = 12$.

7.2. Cylindrical die pressed into a cantilever beam

We repeat the previous example with a different boundary condition in which the now cantilevered slab is fixed over the right rather than the bottom face, cf. Figure 7. Figures 8 and 9 show the optimal designs obtained using the density and B-spline parameterizations, respectively. Table 3 summarizes the numerical results obtained from the $45 \times 20 \times 15$ finite element mesh.

In comparison to the previous fine-mesh case, the density method requires fewer iterations (11 versus 41) and the B-spline method more iterations (23 versus 13), though the total number of iterations for each method remain comparable. In this case, however, the B-spline and density designs have the same performance (attain minimum f_a).

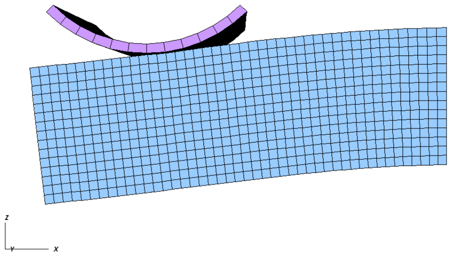

Figure 7: Deformed configuration for the cylindrical die pressed into a cantilever slab.

Table 3: Optimal design summary for cylindrical die pressed into a cantilever slab problem.

Method	$f_a/\lvert f_a^0\rvert$	It.	r_f	# nonzero filter matrix elements	n_d
Density	-0.6974	11	0.7	2 009 512	$13\,500 = 45 \times 20 \times 15$
B-spline	-0.6928	23	-	864 000	$728 = 13 \times 8 \times 7$

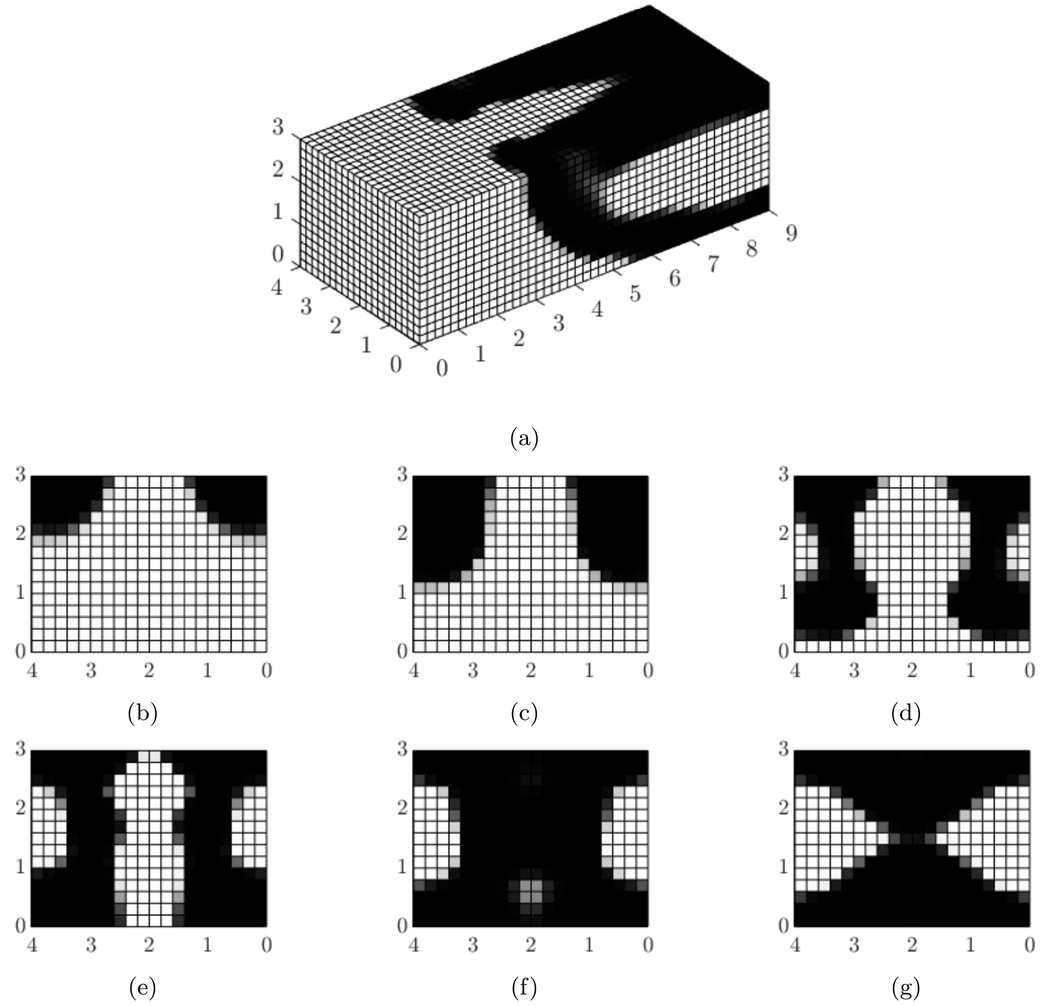

Figure 8: (a) Optimal topology design for cylinder in contact with cantilever slab using the density parameterization. Cuts at (b) $x_1 = 2.75$, (c) $x_1 = 3.5$, (d) $x_1 = 5$, (e) $x_1 = 6$, (f) $x_1 = 7$, and (g) $x_1 = 8$.

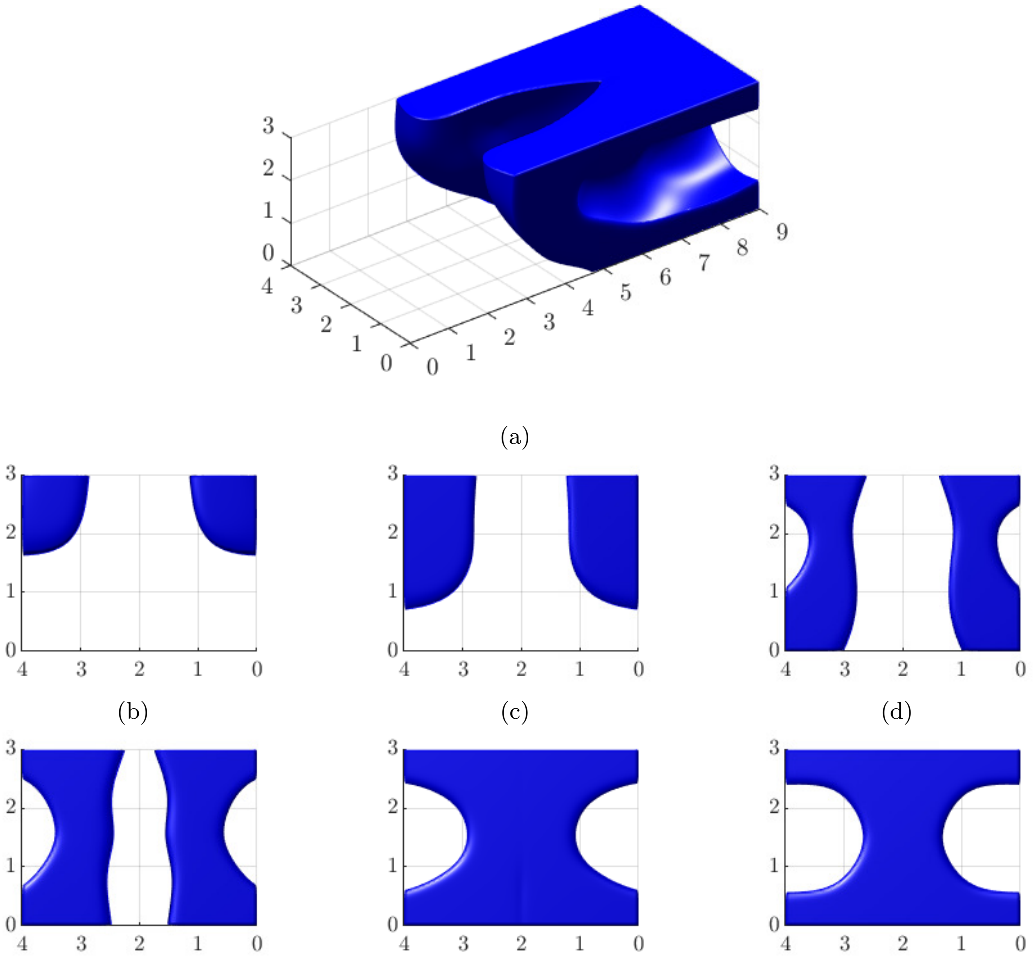

(a)

(b)

(c)

(d)

(e)

(f)

(g)

Figure 9: (a) Optimal topology design for cylinder in contact with cantilever slab using the B-spline parameterization. Cuts at (b) $x_1 = 2.75$, (c) $x_1 = 3.5$, (d) $x_1 = 5$, (e) $x_1 = 6$, (f) $x_1 = 7$, and (g) $x_1 = 8$.

7.3. Contact force

We next maximize the total contact force, cf. Equation (43), solving the same cylindrical die pressed into the rectangular slab from the Subsection 7.1 using exclusively the B-spline method. Figure 10 shows the optimal topology obtained from the 45 × 20 × 15 mesh. As expected, the design is similar as those obtained for maximum strain energy. Figure 11a shows the optimization history for each nodal contact pressure λ_A. Every colored line connects the values of λ_A between successive design iterations. Figure 11b shows the optimization history of the cost function. The contact pressure distribution is smooth as can be seen in Figure 10c. Note that the initial design has a uniform $\nu = 0.4$ volume fraction whereby the SIMP makes the slab very soft which results in small contact pressures ($\Lambda_i \approx 10^{-2}$). The optimization process appears to be smooth even though the pressure Lagrange multipliers switch from active to inactive and vice versa which present significant challenges to the optimization. We attribute this smoothness to the mortar segment-to-segment method, since the nodal contact pressures do not jump appreciably as nodes slide on/off the contact surface.

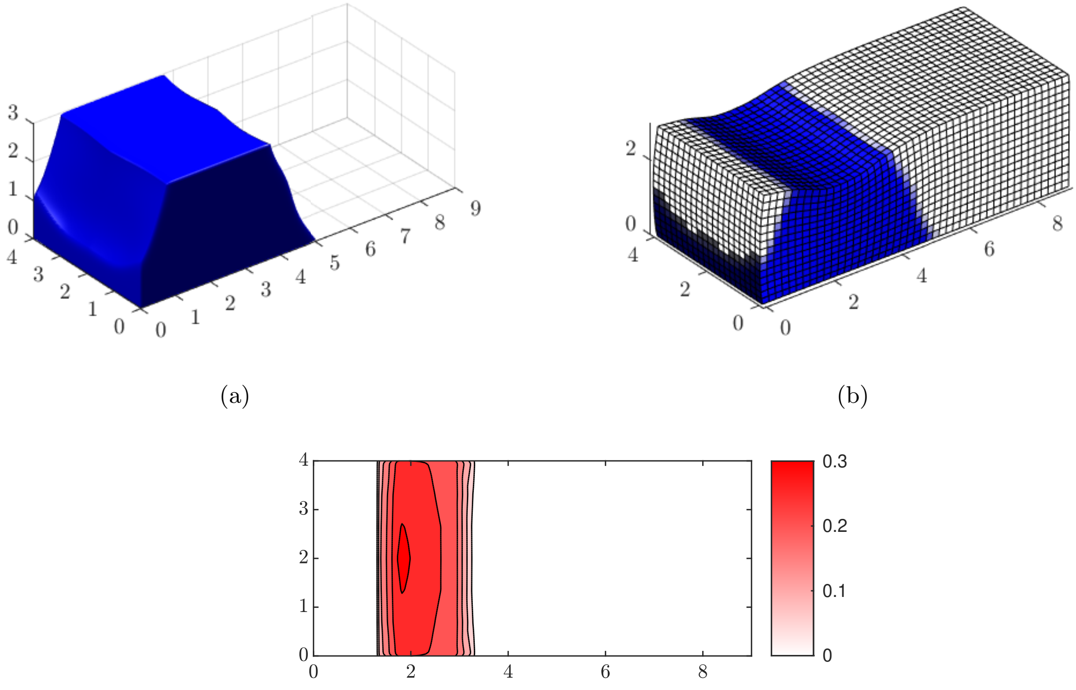

(a)

(b)

(c)

Figure 10: Optimal topology design for maximum total contact force for the cylindrical die pressed into a rectangular slab (a) B-spline zero-level set, (b) deformed configuration, and (c) contact pressure distribution.

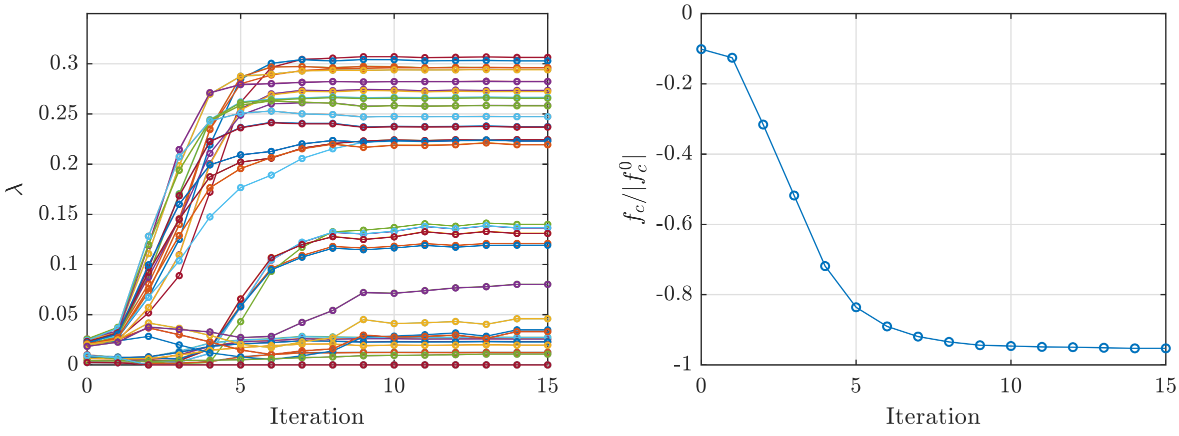

(a) (b)

Figure 11: (a) Nodal pressure Lagrange multipliers and (b) normalized cost function (negative of total contact force) optimization histories for the cylindrical die pressed into rectangular slab problem.

7.4. Sabot

In this final example, we design a sabot, which is a device that ensures the correct position of a cylindrical slug traveling down an oversized annulus, as in the case of a winged projectile traveling down a launch tube. The aluminum slug ($E = 69\text{GPa}$, $\nu = 0.33$) is modeled as a cylinder of radius 25.3mm. We model the sabot as a ring made of fiber reinforced isotropic composite ($E = 6\text{GPa}$, $\nu = 0.33$), whose inner radius (25.4mm) is in contact with the slug and whose the outer radius (50.7mm) is in contact with the annulus. The steel annulus' ($E = 210\text{GPa}$, $\nu = 0.26$) inner and outer radii are 50.8mm and 76.2mm, respectively. The length of each body is 50.8mm and for the purposes of the analysis the axis of the annulus is aligned in the $\mathbf{e}_3$ direction. We fix the radial and tangential displacement on the outside boundary of the annulus. Since we need to constrain axial motion, we can constrain one node per body in this direction. However, we take advantage of domain symmetry and only model the upper half of the domain and impose axial constraints on the bottom surfaces of the three bodies. To prevent rigid body rotations of the slug and the sabot, we constrain motion in the y direction on two points in each body, cf. points A, B, C, and D in Figure 13. The slug can experience a $10000g$ acceleration in any transverse direction, where g is the acceleration of gravity. We mimic the acceleration in the $\mathbf{e}_1$ direction using the inertia relief method. Since our model is frictionless, we do not introduce axial loads. The slug, sabot and barrel are discretized via 10780, 46816, and 13552 finite elements, cf. Figure 13.

To accommodate the unknown loading direction, we enforce cyclic symmetry of the design. In addition, we enforce reflection symmetry about each sector's midplane. To do this, we define the level-set function such that $\phi(r, \alpha) = \phi(r, \alpha^*)$, for $\alpha^* = |\text{mod}(\alpha + \beta/2, \beta) - \beta/2|$, where $\beta = 2\pi/n_p$ and $n_p = 5$ is the number of polar sectors. For example, $\phi(r, \alpha)$ is equal for $\alpha = -10°, 10°, 62°, 82°, 134°, 154°, 206°, 226°, 278°, 298°$, cf. Figure 12. We model ϕ with $396 = 11 \times 6 \times 6$ design variables over a rectangular cuboid grid that encompasses half of the first sector, cf. the gray region in Figure 12. To obtain a "skin" around the design, we enforce the sabot to be solid in the regions where $r < r_i = 28.575\text{mm}$ and $r > r_o = 47.625\text{mm}$. To do this, we define the inner and outer skin level-set functions

$$\begin{aligned} \phi_i(\mathbf{X}) &= m\left(r_i - \sqrt{(\mathbf{X}\cdot\mathbf{e}_1)^2 + (\mathbf{X}\cdot\mathbf{e}_2)^2}\right), \\ \phi_o(\mathbf{X}) &= m\left(\sqrt{(\mathbf{X}\cdot\mathbf{e}_1)^2 + (\mathbf{X}\cdot\mathbf{e}_2)^2} - r_o\right), \end{aligned} \tag{45}$$

where $m = 5$. We then use Boolean operators to define the design level-set function $\tilde{\phi}$ from which the volume fraction ν is evaluated, i.e.,

$$\tilde{\phi}(\mathbf{X}, \mathbf{d}) = \phi(\mathbf{X}, \mathbf{d}) \vee (\phi_i(\mathbf{X}) \vee \phi_o(\mathbf{X})) \ , \tag{46}$$

where $\vee$ is the logical disjunction operator, i.e., max function. We replace the max function with the R-function $\phi_a \vee_o \phi_b = \frac{1}{2}(\phi_a + \phi_b + \sqrt{(\phi_a - \phi_b)^2 + \epsilon_\phi} - \sqrt{\epsilon_\phi})$ which as explained in [64] is positive valued if $\phi_a > 0$ or $\phi_b > 0$. To make this function differentiable at all pairs (ϕ_a, ϕ_b), we add the $\epsilon_\phi = 10^{-4} > 0$ term.

We minimize the compliance and limit the total volume fraction of the sabot to $\nu_{max} = 0.5$. The optimization converges in 25 iterations to a topology that resembles a wheel with hollow spokes, cf. Figure 14.

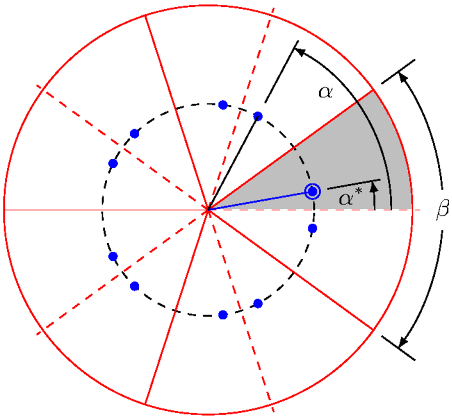

Figure 12: Cyclic symmetry.

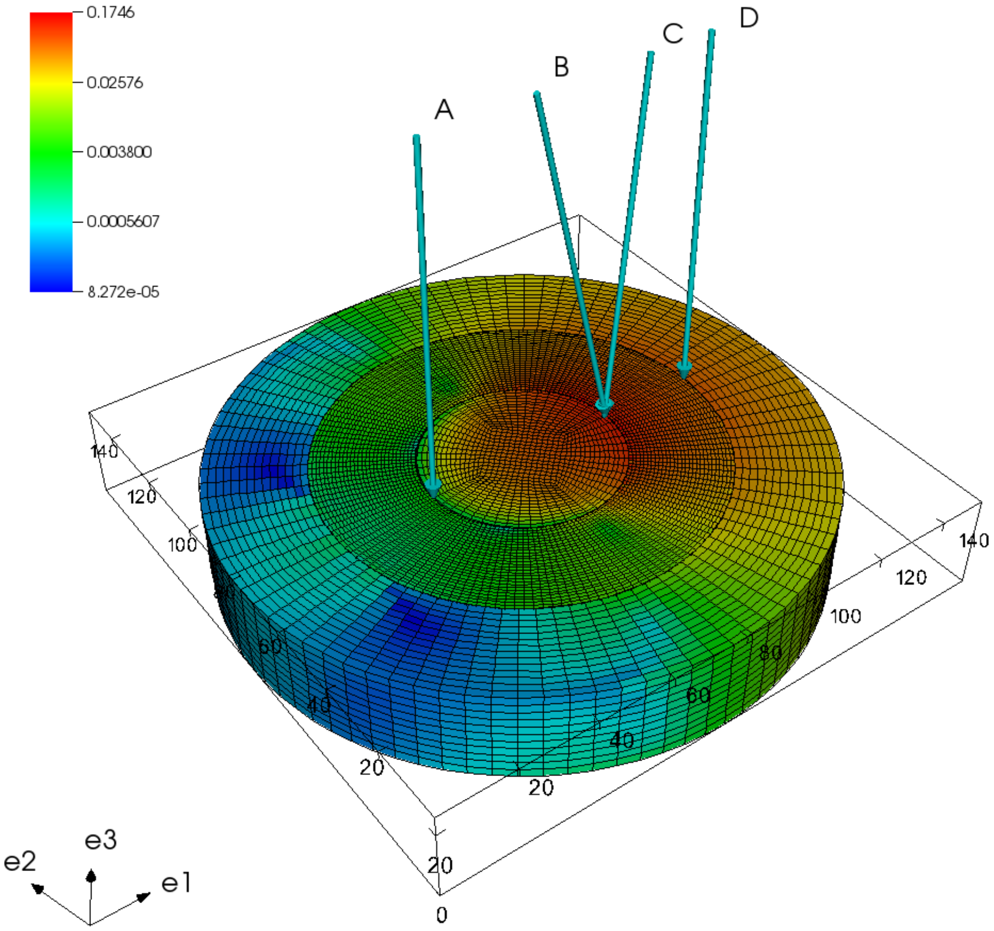

Figure 13: Stress distribution for the nominal design filled with material for the sabot problem.

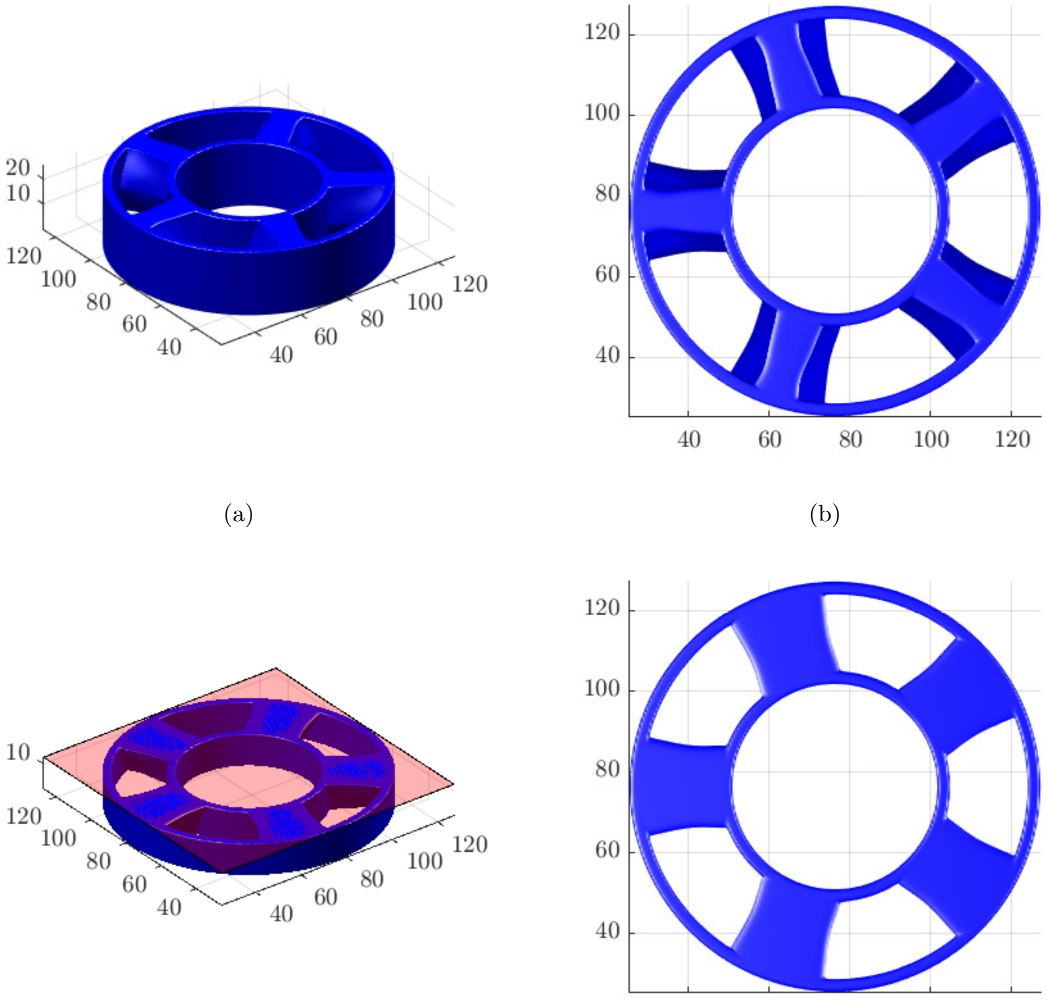

(a) (b)

(c) (d)

Figure 14: Optimal topology design for the sabot problem (a) isometric and (b) top views at $x_3 = 25.4$mm, and (c) isometric and (d) top views cut at $x_3 = 6.3$mm.

8. Conclusions

In this paper, we use state-of-the-art contact and efficient optimization algorithms to solve topology design problems with multiple three-dimensional deformable components in contact. Our simulation is based on a general continuum formulation of the contact model to make it suitable to large deformation problems. To solve the governing equation, we use the ALM due to its robustness and accuracy.

The optimization problem is solved with nonlinear programming algorithms so efficient sensitivity computations are essential. An analytical adjoint sensitivity analysis for general functionals is formulated using the continuum formulation. And because we use the ALM to solve the primal analysis, we also use it to solve the adjoint problem. This requires an iterative solution of the linear adjoint problem. Fortunately, the adjoint analysis reuses the tangent stiffness matrix from the primal analysis and converges quickly.

The mortar segment-to-segment method is used to discretize the contact problem so that the contact forces vary smoothly. As such, the optimization history is well-behaved since the contact pressures do not jump as nodes slide on/off the contact surface.

Our topology optimization uses a B-spline design parameterization independent of the finite element discretization. This representation naturally regularizes the TO problem and ensures satisfaction of an implicit slope constraint that eliminates small features. The B-spline representation also requires fewer design variables compared to the usual element-wise parameterizations. Furthermore, we have a precise description of the design boundary.

Modeling contact allows us to design with more meaningful response measures, e.g., on the total contact force or uniformity of the contact force. Our formulation accommodates such responses. Example problems that maximize the total contact force, maximize the strain energy, and minimize the compliance demonstrate the efficacy of our method.

For future work, the authors will incorporate Coulomb friction [9].

Acknowledgment

Portions of this work were performed under the auspices of the U.S. Department of Energy by Lawrence Livermore National Laboratory (LLNL) under Contract DE-AC52-07NA27344, cf. ref number LLNL-JRNL-787828.

Appendices

A. Total contact force

The surface integral of Equation (43) is computed over the non-mortar (slave) surface $\gamma = \gamma^{(1)}$ as

$$f_c = \sum_{f=1}^{n_f} \int_{\boldsymbol{\xi}} \lambda\left(\mathbf{x}(\boldsymbol{\xi})\right) \left| \frac{\partial \mathbf{x}}{\partial \xi_1} \wedge \frac{\partial \mathbf{x}}{\partial \xi_2} \right| d\boldsymbol{\xi}\,, \tag{A.1}$$

where n_f is the number of finite element facets on the slave surface, $\boldsymbol{\xi}$ is the iso-parametric surface coordinate vector, $\lambda = \mathbf{M}\left(\boldsymbol{\xi}\right) \boldsymbol{\Lambda}_f$ is the pressure Lagrange multiplier field, $\boldsymbol{\Lambda}_f = [\lambda_1, \lambda_2, \lambda_3, \lambda_4]^\top$ is the element facet vector of nodal Lagrange multipliers, $\mathbf{M}(\boldsymbol{\xi}) = [M_1(\boldsymbol{\xi}), M_2(\boldsymbol{\xi}), M_3(\boldsymbol{\xi}), M_4(\boldsymbol{\xi})]$ is the element facet vector of basis functions, $\mathbf{x} = \mathbf{x}_f\, \mathbf{M}^\top(\boldsymbol{\xi})$ is the deformed material point position, $\mathbf{x}_f = [\mathbf{x}_1\ \mathbf{x}_2\ \mathbf{x}_3\ \mathbf{x}_4]$ is the 3×4 matrix of deformed nodal coordinates of the facet f, and for conciseness we drop the superscript "(1)," i.e., $\mathbf{x} = \mathbf{x}^{(1)}$ and $\boldsymbol{\xi} = \boldsymbol{\xi}^{(1)}$. The derivatives of $\mathbf{x}$, i.e., the surface tangent vectors, are

$$\left[\frac{\partial \mathbf{x}}{\partial \xi_1}\ \frac{\partial \mathbf{x}}{\partial \xi_2} \right] = \mathbf{x}_f\, \frac{\partial \mathbf{M}^\top}{\partial \boldsymbol{\xi}} = \mathbf{x}_f\, \tilde{\mathbf{B}}\,, \tag{A.2}$$

where $\tilde{\mathbf{B}}$ is a 4×2 matrix. We rearrange the above in vector form as

$$\begin{bmatrix} \frac{\partial x_1}{\partial \xi_1} \\ \frac{\partial x_2}{\partial \xi_1} \\ \frac{\partial x_3}{\partial \xi_1} \\ \frac{\partial x_1}{\partial \xi_2} \\ \frac{\partial x_2}{\partial \xi_2} \\ \frac{\partial x_3}{\partial \xi_2} \end{bmatrix} = \left(\tilde{\mathbf{B}}^\top \odot \mathbf{I}\right) \operatorname{vec}(\mathbf{x}_f) = \begin{bmatrix} \mathbf{B}_{11} \\ \mathbf{B}_{21} \\ \mathbf{B}_{31} \\ \mathbf{B}_{12} \\ \mathbf{B}_{22} \\ \mathbf{B}_{32} \end{bmatrix} \operatorname{vec}(\mathbf{x}_f) \,, \tag{A.3}$$

where $\odot$ is the Kronecker product, $\mathbf{I}$ is 3 dimensional identity matrix and the $\mathbf{B}_{ij}$ are 1×12 row vectors.

We next define the surface metric

$$s = \left| \frac{\partial \mathbf{x}}{\partial \xi_1} \wedge \frac{\partial \mathbf{x}}{\partial \xi_2} \right| = \sqrt{\left(\frac{\partial x_1}{\partial \xi_1} \frac{\partial x_2}{\partial \xi_2} - \frac{\partial x_1}{\partial \xi_2} \frac{\partial x_2}{\partial \xi_1} \right)^2 + \left(\frac{\partial x_1}{\partial \xi_2} \frac{\partial x_3}{\partial \xi_1} - \frac{\partial x_1}{\partial \xi_1} \frac{\partial x_3}{\partial \xi_2} \right)^2 + \left(\frac{\partial x_2}{\partial \xi_1} \frac{\partial x_3}{\partial \xi_2} - \frac{\partial x_2}{\partial \xi_2} \frac{\partial x_3}{\partial \xi_1} \right)^2} \,, \tag{A.4}$$

to express the derivatives of the total contact force as

$$\frac{\partial f_c}{\partial \mathbf{\Lambda}_f} = \sum_{f=1}^{n} \int_{\boldsymbol{\xi}} \mathbf{M}^\top s \, d\boldsymbol{\xi} \,, \tag{A.5}$$

$$\frac{\partial f_c}{\partial \mathbf{U}_f} = \sum_{f=1}^{n} \int_{\boldsymbol{\xi}} \lambda \frac{\partial s}{\partial \mathbf{U}_f} \, d\boldsymbol{\xi} \,, \tag{A.6}$$

where

$$\begin{aligned} \frac{\partial s}{\partial \mathbf{U}_f} = \frac{1}{s} \Bigg(& \mathbf{B}_{11}^\top \frac{\partial x_2}{\partial \xi_2} + \frac{\partial x_1}{\partial \xi_1} \mathbf{B}_{22}^\top - \mathbf{B}_{12}^\top \frac{\partial x_2}{\partial \xi_1} - \frac{\partial x_1}{\partial \xi_2} \mathbf{B}_{21}^\top + \mathbf{B}_{12}^\top \frac{\partial x_3}{\partial \xi_1} + \frac{\partial x_1}{\partial \xi_2} \mathbf{B}_{31}^\top \\ & - \mathbf{B}_{11}^\top \frac{\partial x_3}{\partial \xi_2} - \frac{\partial x_1}{\partial \xi_1} \mathbf{B}_{32}^\top + \mathbf{B}_{21}^\top \frac{\partial x_3}{\partial \xi_2} + \frac{\partial x_2}{\partial \xi_1} \mathbf{B}_{32}^\top - \mathbf{B}_{22}^\top \frac{\partial x_3}{\partial \xi_1} - \frac{\partial x_2}{\partial \xi_2} \mathbf{B}_{31}^\top \Bigg) \,. \end{aligned} \tag{A.7}$$

Equations (A.5) and (A.6) represent $\int_\gamma \zeta' \delta_\nu \lambda \, \mathrm{d}a$ and $\int_\gamma \zeta \, \mathrm{div}_\gamma \delta_\nu \mathbf{u}^{(1)} \mathrm{d}a$ in Equation (19) respectively.

B. Tri-cubic B-spline

For three-dimensions, the shape functions for uniform tri-cubic B-spline over the $[-1, 1]^3$ domain are obtained from the outer product of the one-dimensional B-spline functions, i.e.,

$$\hat{\mathbf{N}}(\boldsymbol{\xi}) = \left\{ \begin{array}{c} \bar{N}_1(\xi_1)\bar{N}_1(\xi_2)\bar{N}_1(\xi_3) \\ \bar{N}_1(\xi_1)\bar{N}_1(\xi_2)\bar{N}_2(\xi_3) \\ \bar{N}_1(\xi_1)\bar{N}_1(\xi_2)\bar{N}_3(\xi_3) \\ \vdots \\ \bar{N}_4(\xi_1)\bar{N}_4(\xi_2)\bar{N}_4(\xi_2) \end{array} \right\} .$$

If we have a rectangular cuboid domain with uniform $n_x \times n_y \times n_z$ patches, there is a total of $(n_x + 3)(n_y + 3)(n_z + 3)$ control points.

We use an isoparametric mapping to define the level–set function ϕ. Given the physical control point coordinates $\hat{\mathbf{X}}_i = [\hat{\mathbf{X}}_1 \, \hat{\mathbf{X}}_2 \ldots \hat{\mathbf{X}}_{64}]^\top$ for a patch i, and a position $\mathbf{X}$ in the patch, the level–set function ϕ is defined such that

$$\phi(\mathbf{X})|_{\mathbf{X} = \hat{\mathbf{X}}_i^\top \hat{\mathbf{N}}(\boldsymbol{\xi})} = \mathbf{d}_i^\top \hat{\mathbf{N}}(\boldsymbol{\xi}) \,, \tag{B.1}$$

where $\mathbf{d}_i$ is the 64×1 vector of height parameters for the patch i. Since we use a rectangular cuboid domain, the inverse mapping is straight forward

$$\boldsymbol{\xi} = 2\,\mathrm{diag}\left(\frac{1}{h_x}, \frac{1}{h_y}, \frac{1}{h_z}\right)(\mathbf{X} - \mathbf{X}_c) \tag{B.2}$$

where $\mathbf{X}_c$ and h_x, h_y, and h_z are the center location and the edge lengths of the patch in the $\hat{\mathbf{e}}_1$, $\hat{\mathbf{e}}_2$, and $\hat{\mathbf{e}}_3$ directions, Figure B.1.

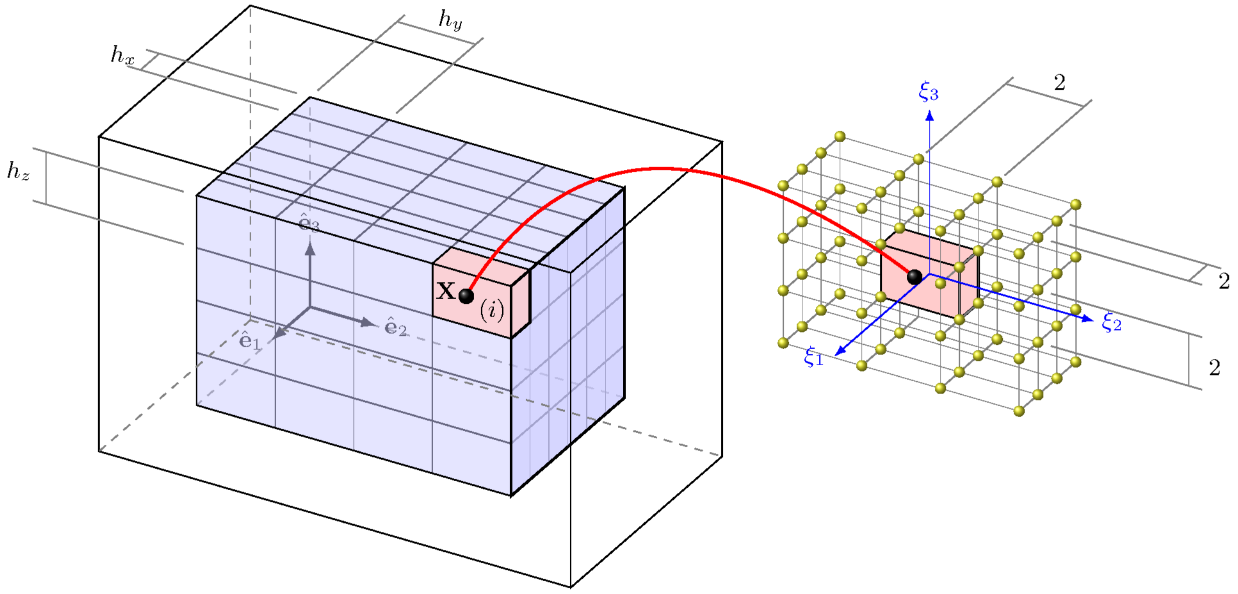

Figure B.1: Rectangular grid of patches in physical coordinates and mapping to the reference coordinate system.

C. Energy functional and stress

In this appendix, we describe the hyperelastic material model used in the examples of this paper. In addition to the relations described in Section 2, we define the isochoric part of $\mathbf{F}$ as $\bar{\mathbf{F}} = J^{-1/3}\mathbf{F}$, i.e., $\det\left(\bar{\mathbf{F}}\right) = 1$. With $\bar{\mathbf{F}}$, we construct $\bar{\mathbf{C}} = \bar{\mathbf{F}}^\top \bar{\mathbf{F}} = J^{-2/3}\mathbf{C}$.

We consider a hyperelastic material that uses the so-called F-bar element formulation presented by Simo and Taylor [65] to provide nearly incompressible behavior while avoiding locking. Using this kinematic description, a Mooney-Rivlin material has the strain energy density functional of the form

$$\hat{W}(\mathbf{C}) = U(J) + \Phi(\mathbf{C}), \tag{C.1}$$

where $U(J)$ and $\Phi(\mathbf{C})$ represent the volumetric and deviatoric parts of $\hat{W}(\mathbf{C})$ respectively. The volumetric part is defined by

$$U(J) \quad = \quad \frac{1}{2}\kappa\,(\ln J)^2 \,, \tag{C.2}$$

where κ is interpreted as the bulk modulus and represents a penalty parameter to achieve incompressibility via the penalty method. The deviatoric part is

$$\Phi(\mathbf{C}) = \hat{\Phi}\left(\bar{I}_1(\bar{\mathbf{C}}), \bar{I}_2(\bar{\mathbf{C}})\right) = A\,\left(\bar{I}_1\left(\bar{\mathbf{C}}\right) - 3\right) + B\,\left(\bar{I}_2\left(\bar{\mathbf{C}}\right) - 3\right)\,, \tag{C.3}$$

where A and B are material coefficients, and $\bar{I}_1\left(\bar{\mathbf{C}}\right) = \mathrm{tr}\left(\bar{\mathbf{C}}\right)$ and $\bar{I}_2\left(\bar{\mathbf{C}}\right) = 1/2[\left(\bar{I}_1(\bar{\mathbf{C}})\right)^2 - \mathrm{tr}\left(\bar{\mathbf{C}}^2\right)]$ are the first and second invariants of $\bar{\mathbf{C}}$. This model differs from the standard Mooney-Rivlin form in that $\bar{I}_1$ and $\bar{I}_2$ are invariants of the deviatoric right Cauchy-Green tensor.

For the finite element implementation, the Jacobian J is replaced with Θ which, to avoid locking, is defined as the average Jacobian over the finite element Ω_e, i.e.,

$$\Theta = \frac{|\omega_e|}{|\Omega_e|}\,. \tag{C.4}$$

In the incompressible limit, the values of J and the relative volume Θ approach unity, and the standard Mooney-Rivlin model is recovered.

The hyperelasticity assumption and objectivity require

$$\begin{aligned} \mathbf{P}(\mathbf{F}) &= \nabla W(\mathbf{F}) \\ &= 2\,\mathbf{F}\,\nabla \hat{W}(\mathbf{C})\,, \end{aligned} \tag{C.5}$$

where $W(\mathbf{F}) = \hat{W}(\mathbf{C})$. As such

$$\begin{aligned} D\mathbf{P}(\mathbf{F}) &= D^2 W(\mathbf{F}) \\ &= 2\,\mathbf{I} \boxtimes \nabla \hat{W} + 4\,(\mathbf{F} \boxtimes \mathbf{I})\,D^2\hat{W}(\mathbf{C})(\mathbf{F} \boxtimes \mathbf{I})^\top\,, \end{aligned} \tag{C.6}$$

where $\boxtimes$ represent the conjugation product with components $(\mathbf{A} \boxtimes \mathbf{B})_{ijkl} = A_{ik}B_{jl}$.

Note that for $\mathbf{C} = \mathbf{I}$, we have zero residual stress as $\nabla \hat{W} = \mathbf{0}$ and the linearized elasticity tensor

$$\mathbb{C} = 4D^2\hat{W}\,|_{\mathbf{C}=\mathbf{I}} \;=\; 4(A+B)\mathbb{I} + \left(\kappa - \frac{4}{3}\,(A+B)\right)\mathbf{I}\otimes\mathbf{I}\,. \tag{C.7}$$

For isotropy $\mathbb{C} = 2\mu\mathbb{I} + \lambda\mathbf{I}\otimes\mathbf{I}$, so for consistency with linear elasticity, it is necessary that the shear modulus is $\mu = 2(A+B)$ and that $\kappa - \frac{4}{3}(A+B) = \kappa - \frac{2}{3}\mu = \lambda$.

References

[1] T. A. Laursen, Formulation and treatment of frictional contact problems using finite elements, Ph.D. thesis, Stanford University (1992).

[2] N. Kikuchi, J. T. Oden, Contact Problems in Elasticity, Society for Industrial and Applied Mathematics, 1988.

[3] T. A. Laursen, Computational Contact and Impact Mechanics: Fundamentals of Modeling Interfacial Problems in Nonlinear Finite Element Analysis, Springer, 2002.

[4] P. Wriggers, T. A. Laursen, Computational contact mechanics, Vol. 2, Springer, 2006.

[5] A. Konyukhov, K. Schweizerhof, Computational Contact Mechanics: Geometrically Exact Theory for Arbitrarily Shaped Bodies, Springer, 2012.

[6] V. A. Yastrebov, Numerical methods in contact mechanics, John Wiley & Sons, 2013.

[7] J. Hallquist, G. Goudreau, D. Benson, Sliding interfaces with contact-impact in large-scale Lagrangian computations, Computer Methods in Applied Mechanics and Engineering 51 (1) (1985) 107 – 137.

[8] M. A. Puso, T. A. Laursen, A mortar segment-to-segment contact method for large deformation solid mechanics, Computer methods in applied mechanics and engineering 193 (6-8) (2004) 601–629.

[9] M. A. Puso, T. A. Laursen, A mortar segment-to-segment frictional contact method for large deformations, Computer methods in applied mechanics and engineering 193 (45-47) (2004) 4891–4913.

[10] I. Nistor, M. L. E. Guiton, P. Massin, N. Mos, S. Gniaut, An X-FEM approach for large sliding contact along discontinuities, International Journal for Numerical Methods in Engineering 78 (12) (2009) 1407–1435.

[11] M. Lawry, K. Maute, Level set shape and topology optimization of finite strain bilateral contact problems, International Journal for Numerical Methods in Engineering.

[12] E. Burman, P. Hansbo, Fictitious domain methods using cut elements: III. A stabilized Nitsche method for Stokes' problem, ESAIM: Mathematical Modelling & Numerical Analysis 48 (3) (2014) 859 – 874.

[13] A. Sharma, K. Maute, Stress–based topology optimization using spatial gradient stabilized XFEM, Structural and Multidisciplinary Optimization 57 (1) (2018) 17–38.

[14] D. Hilding, A. Klarbring, J. Petersson, Optimization of structures in unilateral contact, Applied Mechanics Reviews 52 (4) (1999) 139–160.

[15] A. Klarbring, J. Petersson, M. Rönnqvist, Truss topology optimization including unilateral contact, Journal of optimization theory and applications 87 (1) (1995) 1–31.

[16] J. Petersson, M. Patriksson, Topology optimization of sheets in contact by a subgradient method, International Journal for Numerical Methods in Engineering 40 (7) (1997) 1295–1321.

[17] W. Li, Q. Li, G. P. Steven, Y. Xie, An evolutionary approach to elastic contact optimization of frame structures, Finite Elements in Analysis and Design 40 (1) (2003) 61–81.

[18] E. A. Fancello, Topology optimization for minimum mass design considering local failure constraints and contact boundary conditions, Structural and Multidisciplinary Optimization 32 (3) (2006) 229–240.

[19] M. P. Bendsøe, O. Sigmund, Topology optimization by distribution of isotropic material, Springer, 2004.

[20] B. Desmorat, Structural rigidity optimization with frictionless unilateral contact, International Journal of Solids and Structures 44 (3) (2007) 1132 – 1144.

[21] N. Strömberg, A. Klarbring, Minimization of compliance of a linear elastic structure with contact constraints by using sequentially linear programming and newton's method, in: 7th ASMO UK Conference on Engineering Design Optimization, At Bath, United Kingdom, 2008.

[22] N. Strömberg, A. Klarbring, Topology optimization of structures with contact constraints by using a smooth formulation and nested approach, in: 8th World Congress on Structural and Multidisciplinary Optimization, Lisbon, Portugal, 2009.

[23] N. Strömberg, A. Klarbring, Topology optimization of structures in unilateral contact, Structural and Multidisciplinary Optimization 41 (1) (2010) 57–64.

[24] N. Strömberg, Topology optimization of structures with manufacturing and unilateral contact constraints by minimizing an adjustable compliance–volume product, Structural and Multidisciplinary Optimization 42 (2010) 341–350.

[25] N. Strömberg, The influence of sliding friction on optimal topologies, in: Recent Advances in Contact Mechanics: Papers Collected at the 5th Contact Mechanics International Symposium (CMIS2009), April 28-30, 2009, Chania, Greece, Springer Berlin Heidelberg, Berlin, Heidelberg, 2013, pp. 327–336.

[26] M. Bruggi, P. Duysinx, A stress–based approach to the optimal design of structures with unilateral behavior of material or supports, Structural and Multidisciplinary Optimization 48 (2) (2013) 311–326.

[27] Y. Luo, M. Li, Z. Kang, Topology optimization of hyperelastic structures with frictionless contact supports, International Journal of Solids and Structures 81 (2016) 373–382.

[28] N. D. Mankame, G. K. Ananthasuresh, Topology optimization for synthesis of contact-aided compliant mechanisms using regularized contact modeling, Computers & Structures 82 (15) (2004) 1267 – 1290.

[29] N. Mankame, G. Ananthasuresh, Synthesis of contact-aided compliant mechanisms for non-smooth path generation, International Journal for Numerical Methods in Engineering 69 (12) (2007) 2564–2605.

[30] P. Kumar, R. A. Sauer, A. Saxena, Synthesis of c0 path-generating contact-aided compliant mechanisms using the material mask overlay method, Journal of Mechanical Design 138 (6) (2016) 062301.

[31] P. Kumar, A. Saxena, R. Sauer, Computational synthesis of large deformation compliant mechanisms undergoing self and mutual contact, Journal of Mechanical Design 141 (1) (2019) 012302.

[32] J. Zochowski, A. Sokolowski, Modeling of topological derivatives for contact problems, Numerische Mathematik 1 (102) (2005) 145–179.

[33] A. Myśliński, Topology and shape optimization of contact problems using a level set method, CD ROM Proceedings of VI World Congresses of Structural and Multidisciplinary Optimization. Rio de Janeiro, Brazil 30.

[34] P. Fulmański, A. Laurain, J.-F. Scheid, J. Sokołowski, A level set method in shape and topology optimization for variational inequalities, International Journal of Applied Mathematics and Computer Science 17 (3) (2007) 413–430.

[35] A. Andrade-Campos, A. Ramos, J. Simões, A model of bone adaptation as a topology optimization process with contact, Journal of Biomedical Science and Engineering 5 (05) (2012) 229.

[36] A. Myśliński, Level set method for optimization of contact problems, Engineering Analysis with Boundary Elements 32 (11) (2008) 986–994.

[37] A. Myśliński, Piecewise constant level set method for topology optimization of unilateral contact problems, Advances in Engineering Software 80 (2015) 25–32.

[38] M. Lawry, K. Maute, Level set topology optimization of problems with sliding contact interfaces, Structural and Multidisciplinary Optimization 52 (6) (2015) 1107–1119.

[39] R. Behrou, M. Lawry, K. Maute, Level set topology optimization of structural problems with interface cohesion, International Journal for Numerical Methods in Engineering 112 (8) (2017) 990–1016.

[40] A. Maury, G. Allaire, F. Jouve, Shape optimisation with the level set method for contact problems in linearised elasticity, working paper or preprint (Jan. 2017).

[41] R. R. Mayer, N. Kikuchi, R. A. Scott, Application of topological optimization techniques to structural crashworthiness, International Journal for Numerical Methods in Engineering 39 (8) (1996) 1383–1403.

[42] C. B. Pedersen, Topology optimization design of crushed 2d-frames for desired energy absorption history, Structural and Multidisciplinary Optimization 25 (5-6) (2003) 368–382.

[43] C. B. Pedersen, Topology optimization for crashworthiness of frame structures, International journal of crashworthiness 8 (1) (2003) 29–39.

[44] C. B. Pedersen, Crashworthiness design of transient frame structures using topology optimization, Computer methods in applied mechanics and engineering 193 (6-8) (2004) 653–678.

[45] C. A. Soto, Structural topology optimization for crashworthiness, International Journal of Crashworthiness 9 (3) (2004) 277–283.

[46] J. Forsberg, L. Nilsson, Topology optimization in crashworthiness design, Structural and Multidisciplinary Optimization 33 (1) (2007) 1–12.

[47] N. M. Patel, B.-S. Kang, J. E. Renaud, A. Tovar, Crashworthiness design using topology optimization, Journal of Mechanical Design 131 (6) (2009) 061013.

[48] F. Duddeck, K. Volz, A new topology optimization approach for crashworthiness of passenger vehicles based on physically defined equivalent static loads, in: Int. Crashworthiness Conf. (ICrash), Milano, Italy, 2012.

[49] M. Bujny, N. Aulig, M. Olhofer, F. Duddeck, Evolutionary level set method for crashworthiness topology optimization, in: ECCOMAS Congress 2016, Hersonissos, Greece, 2016.

[50] F. Duddeck, S. Hunkeler, P. Lozano, E. Wehrle, D. Zeng, Topology optimization for crashworthiness of thin-walled structures under axial impact using hybrid cellular automata, Structural and Multidisciplinary Optimization 54 (3) (2016) 415–428.

[51] J. Fang, G. Sun, N. Qiu, N. H. Kim, Q. Li, On design optimization for structural crashworthiness and its state of the art, Structural and Multidisciplinary Optimization 55 (3) (2017) 1091–1119.

[52] X. Qian, Topology optimization in B-spline space, Computer Methods in Applied Mechanics and Engineering 265 (2013) 15–35.

[53] M. Dittmann, M. Franke, I. Temizer, C. Hesch, Isogeometric analysis and thermomechanical mortar contact problems, Computer Methods in Applied Mechanics and Engineering 274 (2014) 192–212.

[54] M. Hiermeier, W. A. Wall, A. Popp, A truly variationally consistent and symmetric mortar-based contact formulation for finite deformation solid mechanics, Computer Methods in Applied Mechanics and Engineering 342 (2018) 532–560.

[55] A. Conn, N. Gould, A. Sartenaer, P. Toint, Convergence properties of an augmented lagrangian algorithm for optimization with a combination of general equality and linear constraints, SIAM Journal on Optimization 6 (3) (1996) 674–703.

[56] P. W. Christensen, A. Klarbring, J. S. Pang, N. Strömberg, Formulation and comparison of algorithms for frictional contact problems, International Journal for Numerical Methods in Engineering 42 (1) (1998) 145–173.

[57] T. E. Bruns, D. A. Tortorelli, Topology optimization of non-linear elastic structures and compliant mechanisms, Computer Methods in Applied Mechanics and Engineering 190 (26) (2001) 3443–3459.

[58] M. Bendsoe, Topology optimization: theory, methods and applications, Springer, 2003.

[59] J. Norato, R. Haber, D. Tortorelli, M. P. Bendsøe, A geometry projection method for shape optimization, International Journal for Numerical Methods in Engineering 60 (14) (2004) 2289–2312.

[60] J. Petersson, O. Sigmund, Slope constrained topology optimization, International Journal for Numerical Methods in Engineering 41 (8) (1998) 1417–1434.

[61] J. C. Simo, T. J. Hughes, Computational inelasticity, Vol. 7, Springer Science & Business Media, 2006.

[62] M. Puso, B. N. Maker, R. M. Ferencz, J. O. Hallquist, NIKE3D: a nonlinear, implicit, three-dimensional finite element code for solid and structural mechanics, Users Manual.

[63] A. Wächter, L. T. Biegler, On the implementation of a primal-dual interior point filter line search algorithm for large-scale nonlinear programming, Mathematical Programming 106 (1) (2006) 25–57.

[64] V. Shapiro, Semi–analytic geometry with R–functions, ACTA numerica 16 (2007) 239–303.

[65] J. C. Simo, R. L. Taylor, Quasi-incompressible finite elasticity in principal stretches. continuum basis and numerical algorithms, Computer methods in applied mechanics and engineering 85 (3) (1991) 273–310.